Jül-4371

Institut für Energie- und Klimaforschung
Plasmaphysik (IEK-4)

B2-B2.5 Code Benchmarking, Part III: Convergence issues of the B2-EIRENE code

Vladislav Kotov, Detlev Reiter

JÜLICH
FORSCHUNGSZENTRUM

B2-B2.5 Code Benchmarking, Part III: Convergence issues of the B2-EIRENE code

Vladislav Kotov, Detlev Reiter

Berichte des Forschungszentrums Jülich; 4371
ISSN 0944-2952
Institut für Energie- und Klimaforschung
Plasmaphysik (IEK-4)
Jül-4371

Zu beziehen durch: Forschungszentrum Jülich GmbH · Zentralbibliothek, Verlag
D-52425 Jülich · Bundesrepublik Deutschland
☎ 02461 61-5220 · Telefax: 02461 61-6103 · e-mail: zb-publikation@fz-juelich.de

Abstract

B2-EIRENE is a finite-volume Computational Fluid Dynamics (CFD) code which describes flow of magnetized charged particles combined self-consistently with kinetic Monte-Carlo (MC) model for neutral particles. The issue of the run-time and accuracy of the coupled package is addressed in the present report. Convergence of different iteration schemes is analyzed in terms of generalized residuals. Particular focus is on the global particle balance. The results and discussions may be of general interest for developers and users of tokamak edge codes based on a CFD-MC combination.

B2-EIRENE ist ein Finite-Volumen Strömungsmechanik (CFD) Code der Strömungen von magnetisierten geladenen Teilchen beschreibt, selbst-konsistent gekoppelt mit einem kinetischen Monte-Carlo (MC) Modell für Neutralteilchen. Der Bericht befasst sich mit dem Problem von Laufzeit und Genauigkeit des gekoppelten Pakets. Numerische Konvergenz von verschiedenen iterativen Verfahren wird analysiert auf Grundlage von verallgemeinerten Residuen. Besonderes Augenmerk wird dabei auf globale Teilchenbilanz gelegt. Ergebnisse und Diskussion können von allgemeinem Interesse sein für Entwickler und Anwender von den auf CFD-MC Kombination basierten Tokamak Randschichtcodes.

Contents

.

Introduction

B2-EIRENE is a computer code which simulates the tokamak plasma edge region and is used to analyze and predict the power and particle exhaust. In particular, one version of this code package (SOLPS4.3) has been extensively applied for the ITER design and scenarios modelling [1]. In B2-EIRENE a fluid (finite-volume) model for plasma (charged particles) is coupled self-consistently with kinetic Monte-Carlo model for neutral particles [2]. The main advantage of the Monte-Carlo (MC) methods is that they can provide physically accurate description of kinetic transport processes in arbitrary complex geometries. Their main drawback is the slow convergence rate - as square root of the number of test particles - due to the statistical character of the solution procedure. Convergence of deterministic numerical methods of Computational Fluid Dynamics (CFD) is easily monitored on the basis of residuals. Ideally, the residuals must reduce exponentially down to the machine precision, see e.g. [3]. It turns out that this strict convergence criterion cannot be fulfilled in many cases of practical relevance if Monte-Carlo is used to calculate the source terms of hydrodynamic equations.

Initially, to reduce the CFD residuals the so called "short runs" of EIRENE were applied [4], with call of the full Monte-Carlo simulation not on all time-iterations using extrapolation of the (physically) accurate neutral solution in-between. This procedure was later substituted by internal iterations of the CFD solver combined with full Monte-Carlo run on each time-iteration. Practical applications have shown that internal iterations allow to reduce the residuals and obtain computationally stable solutions even in conditions of so-called detached divertor plasma. In this regime of operation not only ionization sources, but also volumetric recombination, energy and momentum sources due to interaction of plasma and neutral particles play a significant role. The main disadvantage of this method is a severe restriction posed on the time-step which leads to very long overall run-time of the model (up to several months of wall-clock time for ITER).

This restriction can be lifted if no internal cycling is applied on each time-iteration, but in this case the accuracy of calculations degrades. In how far the solutions obtained with large time-steps are "worse" than the solutions obtained with internal iterations and small time-steps? This is the central question addressed in the present report. To quantify the numerical error a generalized residual (*GENRES*) is introduced for the CFD-MC combination. Solutions obtained for different iteration procedures for real ITER modelling cases are compared in terms of *GENRES*. It can been shown that substantial increase of the number of MC test particles, or, under some circumstances, time-averaging of the source terms, can lead to "fast" (large time-step) solutions with even smaller *GENRES* than in the "reference" computations made with internal iterations.

It turns out, however, that without internal iterations the error in the global balance due to CFD residuals alone can be comparable to the particle throughput which controls the parameters of the divertor plasma, and the solution is driven into completely wrong direction. A correction scheme for the particle balance which still allows large time-steps has been designed and implemented. It was found that this extra correction ("continuity iterations") leads to correct particle balance in the low density (low gas puff rate) ITER test simulations even with relatively small number of MC particles. With high gas puffing rate - hence, dense divertor - continuity iterations lead to increased *GENRES* of the momentum balance equations. However, in the high density case the particle balance issue becomes less critical and continuity iterations

can be can be skipped for main species.

The "ITER-Jülich" version of B2-EIRENE (SOLPS4.3) has been used for prototyping and numerical tests. However, the algorithms and diagnostics described here are general and can be implemented in any branch of B2-EIRENE (SOLPS). The outcomes and discussion can also be of significance for other fusion edge codes based on CFD-MC coupling such as EDGE2D-EIRENE, SOLEDGE/EIRENE or SOLDOR/NEUT2D [5].

Chapter 1

B2-EIRENE: a non-linear multi-physics problem

1.1 Mathematical model

In the numerical experiments discussed in the present report reduced transport equations [6, 7] are used: without drift terms and net electric current. Only steady-state solutions are considered. The set of equations then reads:

$$\mathrm{div}\,(n_\alpha \mathbf{V}_\alpha) = S_n^\alpha + I^\alpha \tag{1.1}$$

$$\mathbf{e}_{||} \cdot \mathrm{div}\,(m_\alpha n_\alpha \mathbf{V}_\alpha \mathbf{V}_\alpha + \Pi_\alpha) =$$

$$= -\mathbf{e}_{||} \cdot \frac{Z_\alpha n_\alpha}{n_e} \nabla(n_e T_e) - \mathbf{e}_{||} \cdot \nabla(n_\alpha T_i) + F_t + \sum_{\alpha'} F_{\alpha\alpha'} + S_u^\alpha \tag{1.2}$$

$$\mathrm{div}\left(2.5 T_e \sum_\alpha Z_\alpha n_\alpha \mathbf{V}_\alpha - k_e \nabla T_e\right) = Q_{ie} + Q_r + S_e \tag{1.3}$$

$$\mathrm{div}\left[2.5 T_i \sum_\alpha n_\alpha \mathbf{V}_\alpha + \sum_\alpha 0.5 m_\alpha V_\alpha^2 n_\alpha \mathbf{V}_\alpha - k_i \nabla T_i + \sum_\alpha \Pi_\alpha \cdot \mathbf{V}_\alpha\right] = -Q_{ie} + S_i \tag{1.4}$$

Here n_α is the number density of the ion fluid α, $\mathbf{V}_\alpha$ is the ion flow velocity, T_e and T_i are the electron and ion temperatures (in energy units), m_α and Z_α are the ion atomic mass and charge number, $n_e = \sum_\alpha Z_\alpha n_\alpha$ is the electron density, I^α is the ion source due to ionization and recombination of other ions, except recombination into atoms (this latter is included in S_n^α, see below), Π_α is the (Newtonian) viscous stress tensor, F_t is the parallel thermal force, $F_{\alpha\alpha'}$ is the parallel friction between ion fluids α and α', k_e and k_i are thermal conductivities of electrons and ions, Q_{ie} is the energy exchange rate between ions and electrons, Q_r is the power radiated by ions (line radiation and bremsstrahlung), $\mathbf{e}_{||}$ is the unit vector parallel to magnetic field $\mathbf{B}$. Equations (1.1) and (1.2) are written for each ion fluid (neutral atoms are excluded), $\sum_\alpha$ and $\sum_{\alpha'}$ implies summation over all ion fluids.

Throughout this document the following terminology is used. An ion type - a type of nucleus - is called "plasma species" or "ion species": D, He, C etc. "Ion fluids" are individual charge-states of the plasma species: He^+, He^{++}, C^{3+} etc.

Equations (1.1)-(1.4) are written in a curvilinear radial-toroidal-poloidal coordinate system, see [8], Chapter 2.3. Assumption of axial symmetry with respect to the tokamak main axis leads to zero toroidal derivatives, and the equations are reduced to 2D in space.

Transport coefficients of plasma along the magnetic field: $k_{e,i}$ and viscosity μ_α, are calculated on the basis of classical theory [9]. They are non-linear functions of plasma parameters and have very strong temperature dependence: $k_{e,i} \sim T_{e,i}^{5/2}$, which makes the whole CFD problem highly non-linear. Another complication from the numerical standpoint is significant anisotropy:

transport coefficients in the cross-field direction are orders of magnitude smaller than the parallel ones. Constant empiric cross-field coefficients are applied in the present work. Equation (1.2) is used only to find the poloidal component u of velocity $\mathbf{V}_\alpha = \mathbf{e}_{||}\frac{B}{B_\theta}u_\alpha + \mathbf{e}_\perp v_\alpha$. Here B_θ is the poloidal component of magnetic field. The component v perpendicular to magnetic surfaces is calculated directly using the convection-diffusion approximation $v_\alpha = -\mathbf{e}_\perp \frac{D_\alpha^\perp}{n_\alpha}\nabla n_\alpha + v_\alpha^{conv}$ with prescribed $D_\alpha^\perp$ and v_α^{conv}.

Equations (1.1)-(1.4) are solved in the plasma edge region - Scrape-off-Layer (SOL) - shown in Figure 1.1. Boundary conditions are specified on the solid surfaces which contact the plasma, and at the boundary with the central plasma region. In particular, total power P_{SOL} and ion flux Γ_{in}^+ (Γ_{in}^α) from the central plasma are prescribed.

Ions which reach the solid surfaces recombine into neutrals: atoms or molecules, which can return to the plasma and interact with charged particles there. The interaction between neutral and charged particles is taken into account in the source terms S_n^α, S_u^α, S_e, S_i of Equations (1.1)-(1.4). The term S_n^α in Equation (1.1) is the net ion source due to ionization of neutrals and volumetric recombination of ions into atoms. S_u^α in Equation (1.2) is the net momentum source of ions (parallel to $\mathbf{B}$) due to their interaction with neutrals: friction force. S_e and S_i in Equations (1.3), (1.4) are energy sources due to elastic and inelastic collisions of charged particles with neutrals. Neutral particles are not confined by magnetic field and can have long mean free paths, therefore, S_n^α, S_u^α, S_e, S_i are calculate with a kinetic Monte-Carlo model - the EIRENE code, see [2] and `www.eirene.de`. The discharge density in the model is controlled by an extra source of neutral particles Γ_{puff} (gas puff), and neutral particles are permanently pumped from the system (Γ_{pump}) to sustain steady-state.

1.2 Numerical procedure

Finite-volume discretization of Equations (1.1)-(1.4) and their boundary conditions [7, 10] has a form of the set of algebraic equations:

$$\mathrm{F}(\phi) = S(\phi) \tag{1.5}$$

Where $\phi = \{n_\alpha, u_\alpha, T_e, T_i\}$, $S = \{S_n^\alpha, S_u^\alpha, S_e, S_i\}$ and F is a non-linear vector function of many variables. Here, distinct from the previous section, n_α, u_α, T_e, T_i, S_n^α, S_u^α, S_e, S_i are vectors $\in \mathbb{R}^N$, where N is the number of grid cells, rather than continuous functions. n_α, u_α, T_e, T_i are values at the cell centers or faces, and S_n^α, S_u^α, S_e, S_i are integrals over the cell.

Equation (1.5) is solved iteratively starting from some initial solution ϕ_0. Time-marching is used to find the steady-state solution through unsteady formulation. On each time-iteration k the solution ϕ_k is sought which obeys the following equation:

$$\mathrm{F}(\phi_k) = \tilde{S}(\phi_{k-1}|\phi_k) + D(\phi_k, \phi_{k-1}) \tag{1.6}$$

Here $D(\phi_k, \phi_{k-1})$ is the time-relaxation (inertia) term - discrete time derivative: $D(\phi_k, \phi_k) = 0$. E.g. for Equation (1.1): $D(\phi_k, \phi_{k-1}) = \frac{n_\alpha^k - n_\alpha^{k-1}}{\Delta t}$, where Δt is the time-step.

The notation $\tilde{S}(\phi_{k-1}|\phi_k)$ introduced in Equation (1.6) has the following special meaning. The Monte-Carlo code EIRENE solves a linear transport problem on the plasma background ϕ_{k-1} as input. Trajectories of atoms and molecules (e.g. D, D_2) are sampled taking into account various kinds of collisions with electrons and ions (ionization, dissociation, charge-exchange, elastic) and solid surfaces. The sources $\tilde{S}(\phi_{k-1})$ are updated during the sampling using track-length and collisional estimators. Tilde in the notation stress out that the Monte-Carlo estimate of the sources contains statistical error, as opposed to $S(\phi)$ which means "exact" value of the sources calculated on plasma state ϕ. That is, the solution which would be found with infinite number of MC test particles. In the course of the solution of Equation (1.6) sources $\tilde{S}(\phi_{k-1})$ can be modified, e.g. re-scaled to fulfill the global particle balance (see below). This correction is reflected in the notation $\tilde{S}(\phi_{k-1}|\phi_k)$.

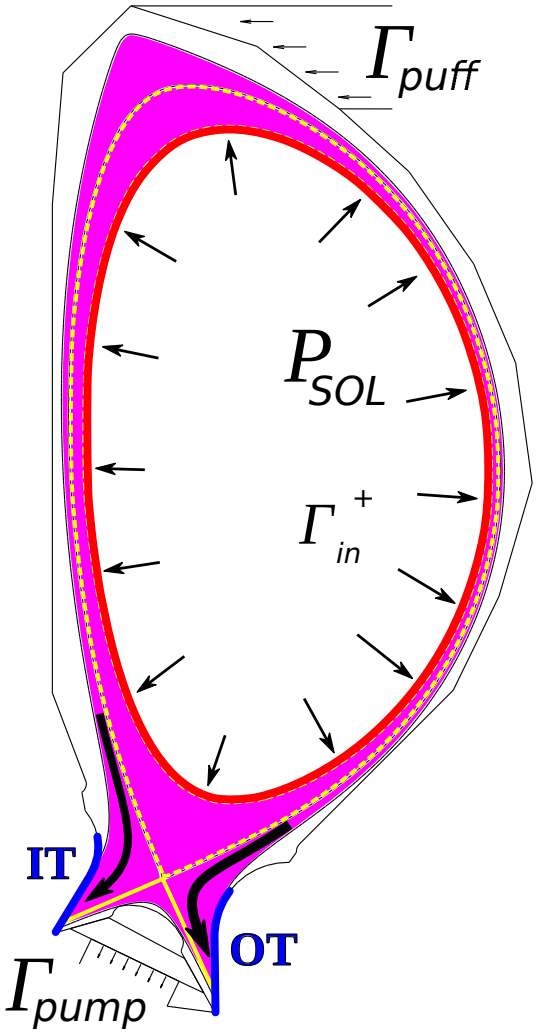

Figure 1.1: Computational domain of B2-EIRENE for ITER: poloidal cross-section. Solid region is SOL where Equations (1.1)-(1.4) are solved. Arrows sketch out the power flow from central plasma to the divertor targets. IT stands for Inner Target and OT for Outer Target respectively. Bold yellow line is the magnetic separatrix.

An extra iteration loop on each time-iteration: "internal iterations", is used to find the approximate solution of Equation (1.6). One each internal iteration a block Gauss-Seidel scheme is applied to update the solution. That is, the fields n_α, u_α, T_e, T_i are updated by solving one by one equations for corrections based on the individual Equations (1.1)-(1.4). The correction ξ is calculated from the linearized form of the discretized equations as follows:

$$\mathrm{M}\left(\phi_k\right)\xi = S\left(\phi_k^{j-1}\right) - \mathrm{M}\left(\phi_k^{j-1}\right)\psi_k^{j-1} = R_k^{j-1}, \quad \psi_k^j = \psi_k^{j-1} + r\xi \tag{1.7}$$

Here $\mathrm{M}\left(\phi\right)$ is a matrix with coefficients dependent on ϕ, ψ is n_α or u_α or T_e or T_i, R_k^{j-1} is the residual, and $0 < r \leq 1$ is the underrelaxation factor. Correction ξ is found as a solution of the set of linear equations, initial value $\phi_k^0 = \phi_{k-1}^m$ where m is the index of last internal iteration. Pseudocode of the internal iteration $j+1$ looks as follows (the time-iteration index k is omitted):

1. Calculating source terms and coefficients
2. Defining boundary conditions as sources in so called guard (boundary) cells
3. Momentum balance, Equation (1.2), for each α: $u_\alpha^{j+1/4} = u_\alpha^j + r\xi$
4. Momentum balance for sum of Equations (1.2) over α:
   $u_\alpha^{j+2/4} = u_\alpha^{j+1/4} + r\xi$
5. Particle balance, Equation (1.1), for each α:
   $n_\alpha^{j+1/2} = n_\alpha^j + r\xi$, $u_\alpha^{j+3/4} = u_\alpha^{j+2/4} - rC\frac{\partial \xi}{\partial x}$
6. Electron energy, Equation (1.3): $T_e^{j+1/2} = T_e^j + r\xi$
7. Ion energy, Equation (1.4): $T_i^{j+1/2} = T_i^j + r\xi$
8. Sum of Equations (1.3) and (1.4): $T_e^{j+1} = T_e^{j+1/2} + r\xi$, $T_i^{j+1} = T_i^{j+1/2} + r\xi$
9. Repeating particle balance, Equation (1.1), for each α:
   $n_\alpha^{j+1} = n_\alpha^{j+1/2} + r\xi$, $u_\alpha^{j+1} = u_\alpha^{j+3/4} - rC\frac{\partial \xi}{\partial x}$

Handling of momentum and continuity equations which includes velocity correction $C\frac{\partial \xi}{\partial x}$ follows the compressible version of the pressure correction algorithm SIMPLE by Patankar, see [10], Chapter 6.7. Its implementation in B2 is described in [7], Chapter 3. This algorithm ensures computational stability at both high and low Mach numbers.

The macroscopic flow chart of the coupling between the CFD part (B2) and MC part (EIRENE) is shown in Figure 1.2. In this flow-chart a single "internal iteration" is the sequence of steps described above.

EIRENE typically uses stratified sampling, see [11], Chapter 10.3. That is, $\tilde{S}$ is calculated as a sum of contributions from N_s sources (strata) sampled independently $\tilde{S} = \sum_{s=1}^{N_s} \tilde{S}^s$. There are four types of primary sources of neutrals in B2-EIRENE: i) recombination of ions on the solid surfaces - recycling sources; ii) volumetric recombination of ions in plasma; iii) external gas puff; iv) sputtering from the solid surfaces. The system in question: SOL and divertor plasma, has very low tolerance with respect to the errors in particle balance - especially in reactor conditions, see [1]. Therefore, to avoid too strong violation of particle balance the total strength of EIRENE recycling strata has to change as the primary source - ion flux to the surfaces - changes in the course of internal iterations of B2. Therefore, as the solution ϕ is modified the particle sources are re-scaled as follows:

$$\tilde{S}_n^\alpha\left(\phi_k^0|\phi_k^j\right) = \sum_s \lambda_s^\beta \tilde{S}_n^{\alpha,s}\left(\phi_k^0\right), \quad \lambda_s^\beta = \frac{Q_s^\beta\left(\phi_k^j\right)}{Q_s^\beta\left(\phi_k^0\right)} \tag{1.8}$$

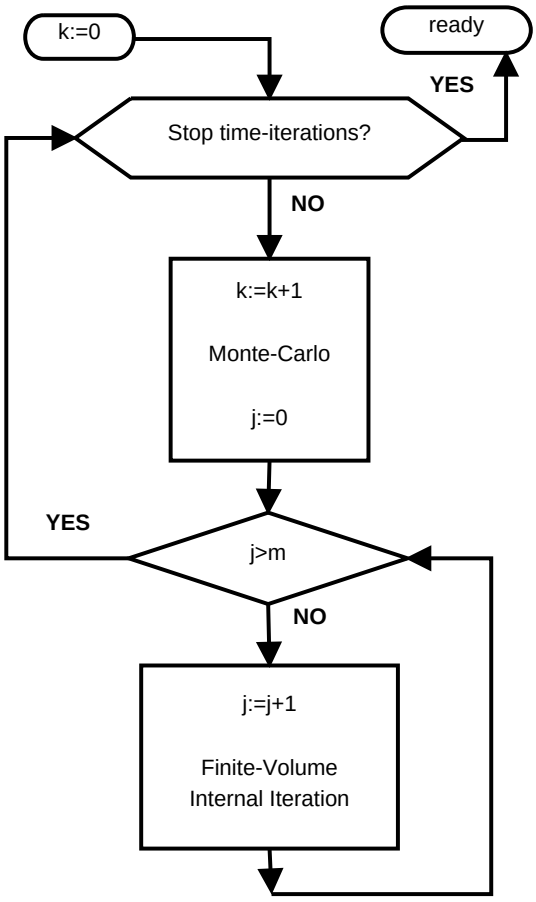

Figure 1.2: Macroscopic flow-chart of the B2-EIRENE code

Here Q_s^β is the sink (flux) of plasma species β in B2 to which the source $S_n^{\alpha,s}$ is proportional. E.g. if α is He^+ and s is a recycling stratum, then Q_s^β is the total flux of He^+ and He^{++} ions to the plasma facing surfaces. For volumetric recombination (and gas puff) λ_s^β is formally set to 1[1].

1.3 Numerical diagnostics

In the present report only steady-state solutions are considered and analyzed. Strictly speaking, the CFD-MC combination never reaches a complete steady-state because Monte-Carlo noise and thus oscillations always remain in the solution. Here a practical definition of "steady-state" is used which is based on the estimated time-scales of selected parameters. The characteristic time-scale τ_X of parameter X is calculated from the time-trace $X(t)$ by fitting it with a linear function:

$$\ln X = \tau_X^{-1} t + C, \quad \frac{1}{\tau_X} = \frac{1}{X}\frac{dX}{dt}$$

The number of last data-points used for the fit in this report is equal to $\max\left(2000, N_p^{(5\ \mu s)}\right)$, where $N_p^{(5\ \mu s)}$ is the number of points which cover last 5 μs of physical time. The same data-points are used to calculate $\Delta\Gamma$ and ΔP below.

The control parameters for which τ_X is calculated are the total amount of ions N_β of species β, total energy in the electrons E_e and ions E_i:

$$N_\beta = \int \sum_{\alpha'} n_{\alpha'} dV, \quad E_e = 1.5 \int n_e T_e dV, \quad E_i = \int \left(1.5 \sum_\alpha n_\alpha T_i + 0.5 \sum_\alpha m_\alpha n_\alpha V_\alpha^2\right) dV$$

(the integration is performed over the whole B2 grid, $\sum_{\alpha'}$ is the sum over all ion fluids of species β), as well as plasma parameters averaged along the magnetic separatrix: $< n_e >^{sep}$, $< T_e >^{sep}$, $< T_i >^{sep}$.

In addition, errors in the global particle and power balance are checked. The relative error in the steady-state particle balance for each species is written as:

$$\Delta\Gamma = \frac{\Gamma_{puff} + \Gamma_{in}^+ - \Gamma_{pump} - \Gamma_{out}^n}{\Gamma_{puff} + \Gamma_{in}^+} \tag{1.9}$$

Here Γ_{puff} is the (atomic) rate of gas puffing, Γ_{in}^+ is the ion influx from central (core) plasma, Γ_{pump} is the (atomic) flux absorbed on the surfaces (pumped), Γ_{out}^n is the flux of atoms to the central plasma (see Figure 1.1).

The relative error in the steady-state power balance:

$$\Delta P = \frac{P_{SOL} - P_{PFC}^+ - P_{PFC}^n - P_{rad} - P_{core}^n}{P_{SOL}} \tag{1.10}$$

Here P_{SOL} is the power influx to the computational domain from central plasma, P_{PFC}^+ is the power deposited by charged particles to the Plasma Facing Components (PFC) - solid surfaces surrounding the plasma, P_{PFC}^n is the power deposited by neutral particles to PFC, P_{rad} is the power radiated from plasma, P_{core}^n is the power transferred by neutral particles back to the central plasma.

[1]There is an option to re-scale volume recombination as well. In the tests described in this report it was found that in low density discharges - when volumetric recombination is weak - correction of this stratum has practically no effect on the resulting convergence behavior. In the tests where recombination is significant this correction was found to increase the error and was therefore switched off (`lstrascl` is set to 0 for volume recombination strata)

Chapter 2

Generalized residual

2.1 General concept

Approximate solution ϕ_k^m can be inserted back into Equation (1.6) to calculate the residual R_k^m:

$$R_k^m = \mathrm{F}\left(\phi_k^m\right) - \tilde{S}\left(\phi_k^0 | \phi_k^m\right) - D\left(\phi_k^m, \phi_k^0\right) \tag{2.1}$$

Equation (2.1) can also be formally re-written as:

$$\mathrm{F}\left(\phi_k^m\right) = S\left(\phi_k^m\right) + \tilde{R}, \quad \tilde{R} = R_k^m + \tilde{S}\left(\phi_k^0 | \phi_k^m\right) - S\left(\phi_k^m\right) + D\left(\phi_k^m, \phi_k^0\right) \tag{2.2}$$

That is, instead of solution ϕ^* of Equation (1.5) the solution ϕ_k^m of Equation (2.2) is found. Note that $S\left(\phi_k^m\right)$ is the "exact" source - as it would be calculated with infinite number of test particles. $S\left(\phi_k^m\right)$ cannot be known in the calculations made with finite number of MC test particles, and only an estimate of this quantity $\tilde{S}\left(\phi_k^m\right)$ - which contains statistical error - can be calculated. Therefore, for $\tilde{R}$ only an estimate can be found as well, but not its exact value.

It sounds plausible that ϕ_k^m should come close to ϕ^* if $\tilde{R}$ is "small enough". Convergence of ϕ_k^m to ϕ^* can be easily shown in a strict way if $H\left(\phi\right) = S\left(\phi\right) - \mathrm{F}\left(\phi\right) + \phi$ forms a contractive mapping. That is, for any ϕ_1, ϕ_2 belonging to the domain of interest:

$$\left\| H\left(\phi_1\right) - H\left(\phi_2\right) \right\| \leq \delta \left\| \phi_1 - \phi_2 \right\| \tag{2.3}$$

With a parameter δ: $0 < \delta < 1$. Therefore, since $\phi^* = H\left(\phi^*\right)$ and $\phi_k^m = H\left(\phi_k^m\right) + \tilde{R}$:

$$\left\| \phi_* - \phi_k^m \right\| = \left\| H\left(\phi^*\right) - H\left(\phi_k^m\right) - \tilde{R} \right\| \leq \delta \left\| \phi_* - \phi_k^m \right\| + \left\| \tilde{R} \right\| \Rightarrow \left\| \phi_* - \phi_k^m \right\| \leq \frac{1}{1-\delta} \left\| \tilde{R} \right\| \tag{2.4}$$

That is, the distance between approximate and exact solutions is reduced when $\left\| \tilde{R} \right\|$ is reduced. According to the contraction mapping theorem, see [12], Chapter 5.1.3, fulfillment of condition (2.3) with $\delta < 1$ is also *sufficient* for existence of a unique solution of Equation (1.5).

An estimate of $\left\| \tilde{R} \right\|$ can serve as a diagnostic (measure) of convergence. It is convenient to split $\left\| \tilde{R} \right\|$ into two parts:

$$\left\| \tilde{R} \right\| \leq G = R + \Delta S \tag{2.5}$$

Where

$$R = \left\| R_k^m \right\|, \quad \Delta S = \left\| \tilde{S}\left(\phi_k^0 | \phi_k^m\right) - S\left(\phi_k^m\right) + D\left(\phi_k^m, \phi_k^0\right) \right\| \tag{2.6}$$

G defined by Equation (2.5) is called here the *generalized residual*. R is the error related to the inaccuracy of solving the set of algebraic equations (1.6) - the standard CFD residual. ΔS is the error which occurs: a) because of statustical noise and b) because the sources are calculated by the Monte-Carlo model for "old" ϕ_k^0, but not for "up-to date" ϕ_k^m. The (discrete) time derivative

is included in ΔS as well. It is to be expected that if the steady-state solution is almost reached, then both non zero $D\left(\phi_k^m, \phi_k^0\right)$ and $\tilde{S}\left(\phi_k^0|\phi_k^m\right) - S\left(\phi_k^m\right)$ are caused mainly by the statistical noise in $\tilde{S}$. This is the rationale for combining those two terms in one norm.

The term ΔS without time-derivative can be called the source inconsistency or operator splitting error. With finite number of test particles exact value of ΔS is not known, and only its estimate can be calculated:

$$\Delta\tilde{S} = \left\| \tilde{S}\left(\phi_k^0|\phi_k^m\right) - \tilde{S}\left(\phi_k^m\right) + D\left(\phi_k^m, \phi_k^0\right) \right\| \tag{2.7}$$

However, with certain confidence the error $E\left(\Delta S\right) = \left|\Delta S - \Delta\tilde{S}\right|$ can be estimated using statistical methods.

It is readily seen that the discussion in this section is applicable to any numerical algorithm which can be described in the form of Equation (1.6).

2.2 Implementation in B2-EIRENE

Implementation of generalized residual, Equations (2.5), (2.6), in the B2-EIRENE code is based on l_1-norm: $\|X\|_1 = \sum_{i=1}^{N} |x_i|$. This norm has a convenient property that if $X = \{X_1 ... X_\gamma ... X_M\}$, then $\|X\|_1 = \sum_{\gamma=1}^{M} \|X_\gamma\|_1$. Therefore, G can be split into contributions for individual equations:

$$G = \sum_\alpha G_n^\alpha + \sum_\alpha G_u^\alpha + G_e + G_i = \sum_{\gamma=\left\{{}_n^\alpha, {}_u^\alpha, e, i\right\}} G_\gamma, \quad G_\gamma = R_\gamma + \Delta S_\gamma \tag{2.8}$$

Where R_γ and ΔS_γ are calculated according to Equations (2.1) and (2.6) with $\mathrm{F}\left(\phi_k^m\right) = \left\{\mathrm{F}_\gamma\left(\phi_k^m\right)\right\}$, $D\left(\phi_k^m, \phi_k^0\right) = \left\{D_\gamma\left(\phi_k^m, \phi_k^0\right)\right\}$, $\tilde{S}\left(\phi_k^0|\phi_k^m\right) = \left\{\tilde{S}_\gamma\left(\phi_k^0|\phi_k^m\right)\right\}$ and $S\left(\phi_k^m\right) = \left\{S_\gamma\left(\phi_k^m\right)\right\}$ replaced by $\mathrm{F}_\gamma\left(\phi_k^m\right)$, $D_\gamma\left(\phi_k^m, \phi_k^0\right)$, $\tilde{S}_\gamma\left(\phi_k^0|\phi_k^m\right)$ and $S_\gamma\left(\phi_k^m\right)$ respectively. Indexes ${}_n^\alpha$, ${}_u^\alpha$, e, i stand for particle, momentum, electron and ion energy balance.

Equation for the generalized residual G_γ with error bars reads as follows:

$$G_\gamma = R_\gamma + \Delta\tilde{S}_\gamma + \begin{cases} +3\sigma_\gamma \\ -\min\left(3\sigma_\gamma, \Delta\tilde{S}_\gamma\right) \end{cases} \tag{2.9}$$

Here:

$$\sigma_\gamma = \sqrt{\sum_{i=1}^{N} \left(\sigma_i\left(S_\gamma\right)\right)^2} \tag{2.10}$$

is the mean square of the standard deviations (sample standard deviation of the mean) in the grid cells i which approximates the standard deviation of $\Delta\tilde{S}_\gamma$. Expression $\min\left(3\sigma_\gamma, \Delta\tilde{S}_\gamma\right)$ takes into account that $\Delta S_\gamma \geq 0$. Equation (2.9) is written for confidence interval 0.997 assuming Gaussian distribution of error. Equation (2.10) is strictly valid only if S_γ calculated in different cells are completely uncorrelated. To estimate the effect of correlation the standard deviations of $\|S_\gamma\|_1$ are also calculated and compared to Equation (2.10). For the test case '1e-4/1/1' from Section 4.1 below the ratio between σ_γ calculated using Equation (2.10) and the standard deviation of $\|S_\gamma\|_1$ is 0.77 at worst. For the case '3e-7/20/1' from Section 4.2 the worst case ratio is 0.43 (He momentum sources).

For practical evaluations it is more convenient to use the normalized (dimensionless) form of G_γ:

$$\hat{G}_\gamma = G_\gamma \Big/ \left\|\tilde{S}_\gamma\left(\phi_k^m\right)\right\|_1 \tag{2.11}$$

In the text below the normalized residual $\hat{G}_\gamma$ is often referred to as *GENRES*.

G_γ should not be mixed up with errors in the particle, momentum and energy balances. Those latter are the absolute values of the sums of contributions in the individual cells - not the sums of the absolute values, and they are $\leq G_\gamma$.

G_γ based on l_1-norm can be easily further decomposed into residuals of individual regions of the computational domain to analyze them separately.

Chapter 3

Time averaging of source terms

B2-EIRENE experience shows that internal iterations, $m > 1$, are required to reduce the residual R. However, this procedure restricts the time-step, therefore, a very large number of time-iterations is needed to reach the steady-state solution. Too large time-step can lead to divergence of the internal iterations and hence numerical instability. With $m = 1$ the simulation can be stable with much larger time-steps. "Stable", in the sense that a steady-state solution is reached. However, R, thus, *GENRES* are much larger in this case then those obtained with $m > 1$ and a small time step. Specific examples will be discussed below in Section 5.

It turns out that R can be also significantly reduced if the source term calculated in the Monte-Carlo run $\tilde{S}\left(\phi_k^0\right)$ is replaced by an average over past L_k time-iterations:

$$\tilde{S}\left(\phi_k^0\right) \to \bar{S}^k = \frac{1}{L_k}\sum_{l=1}^{L_k}\tilde{S}\left(\phi_{k-L_k+l}^0\right), \quad L_k = \mathrm{mod}\left(k-1, L\right)+1 \tag{3.1}$$

That is, the averaging is restarted every L time-iterations where L is an input parameter. According to ref. [5] this particular time-averaging is applied in the code SOLDOR/NEUT2D.

It can be easily shown that the variation of $\bar{S}^k$ between two subsequent time-iterations is much smaller than that of the original source terms $\tilde{S}\left(\phi_k^0\right)$. Indeed, if $\|S_i - S_j\| < \delta$, $k-L_k+1 \le i,j \le k$, then for $L_k > 1$:

$$\left\|\bar{S}^k - \bar{S}^{k-1}\right\| = \left\|\frac{1}{L_k}\sum_{l=1}^{L_k} S_l - \frac{1}{L_k-1}\sum_{l=1}^{L_k-1} S_l\right\| = \left\|\frac{\sum_{l=1}^{L_k-1}\left(S_{L_k}-S_l\right)}{L_k\left(L_k-1\right)}\right\| < \frac{\delta}{L_k}$$

In practice the reduction of $\left\|\bar{S}^k - \bar{S}^{k-1}\right\|$ with increased L_k leads to reduction of R, an example is shown in Figure 4.3 below. The minimum of R is reached roughly on the time-iteration for which $L_k = L$. It makes sense, therefore, to consider the solution only on those time-iterations, and to check *GENRES* only on those time-iterations as well.

The error bar of the estimate of $\Delta\tilde{S}$, see Equations (2.7) and (2.9), can also be significantly reduced with moderate increase of the computational time. Increasing the number of test particles when calculating $\tilde{S}\left(\phi_k^m\right)$ by a factor of f_{MC} reduces the statistical error by a factor of $\approx \sqrt{f_{MC}}$. At the same time, if the number of particles is increased only for $k:\ L_k = L$, then the total time spent for particle sampling is increased by only a factor of $\left(L-1+f_{MC}\right)/L$. E.g. for $f_{MC} = L/2+1$ the accumulated Monte-Carlo time is increased by only 50 %.

To achieve better particle balance, instead of Equation (1.8) the averages of sources normalized to the total source strength Q_s^γ for each stratum s are accumulated:

$$\bar{S}_\gamma^k = \frac{1}{L_k}\sum_{s=1}^{N_s} Q_\gamma^s\left(\phi_k^0\right)\sum_{l=1}^{L_k}\frac{\tilde{S}_s^\gamma\left(\phi_{k-L_k+l}^0\right)}{Q_\gamma^s\left(\phi_{k-L_k+l}^0\right)} \tag{3.2}$$

For particle sources, $\overset{\gamma=\alpha}{n}$, Q_s^γ is the same as Q_s^β in Equation (1.8). The same scaling is used for momentum, $\overset{\gamma=\alpha}{u}$ as well. Energy sources, $\gamma = e, i$ are scaled with total ion fluxes: sum over all

α. Averaging described by Equation (3.2) is used in the tests described in the next section for all types of source terms: S_n^α, S_u^α, S_e and S_i. It was found critical to use this kind of averaging for particle sources S_n^α. At the same time, for other types of sources no significant difference between applying the Equation (3.1) or Equation (3.2) was revealed.

Chapter 4

Test runs

4.1 Single fluid test

In this section different modes of operation of B2-EIRENE are analyzed in terms of generalized residuals. The tests are made for virtual discharge #2013vk4 from the ITER database of B2-EIRENE runs [13]. Geometry and magnetic configuration of the model is shown in Figure 1.1. D^+ is the only ion species in the model plasma. Total power input from the central plasma P_{SOL}=38 MW. Set of atomic and molecular processes applied in the neutral transport code is the same as that described in [14], excluding neutral-neutral collisions and opacity of line radiation.

Intensity of interaction between neutral and charged particles in front of the divertor targets is known to strongly depend on the neutral pressure at the the entrance to the pump duct p_{PFR} [1]. For the discharge in question p_{PFR}=3 Pa. At such low pressure the plasma temperature in front of the targets is relatively high: one speaks of "attached divertor". From the point of view of numerical solution that means relatively low importance of the momentum source S_m, and low rate of volumetric recombination compared to recombination of ions on the plasma facing surfaces.

Numerical settings of the test runs are listed in Table 4.1. In this table Δt is the time step, m is the number of internal iterations, L is the maximum number of terms in the time-average, Equation (3.2), f_{MC} is the multiplier for the number of test particles. All cases reach steady-state solution with characteristic decay times τ >10 sec, see Section 1.3 for definition.

An example of the time evolution of generalized residuals is shown in Figure 4.1. The run is started from a non-converged initial solution. After initial perturbation the residuals saturate, and only weak oscillations remain. Diagrams of normalized generalized residuals $\hat{G}_\gamma$ recorded on the last time-iteration are shown in Figure 4.2. For tests with $L > 1$ this last iteration is the one for which $L_k = L$. Numerical values of individual contributions to $\hat{G}_\gamma$ can be found in Table 4.2.

For simulations of ITER edge plasma the B2-EIRENE code is typically used with $m > 1$ (m=15..20). This mode apparently ensures smallest residuals R compared to others which have been tried so far. With $m = 1$, which allows larger Δt, the residuals $\hat{G}_\gamma$ are larger, mainly because of much larger R. Averaging, Equation (3.2), reduces both R and ΔS, making G even smaller then that calculated with $m > 1$. In the runs with $L > 1$ the number of test-particles on the time-iterations k : $L_k = L$ was multiplied by a factor of $L/2$, which is the reason of significant reduction of σ for those cases. In the $m = 1$ case both R and ΔS can be also reduced by increasing the number of Monte-Carlo particles on each time-iteration. However, the reduction of R in this case is far less pronounced than with $L > 1$.

The action of averaging is demonstrated in Figure 4.3, where behavior of residuals R_γ in the course of time-iterations is shown. Their decrease on the time averaging phase is clearly seen. Although averaging helps to significantly decrease R_γ, those residuals are still orders of magnitude larger than what can be achieved with internal iterations, see Table 4.2. At the same

Table 4.1: Numerical settings of the single fluid test cases (#2013vk4)

Notation	Δt, sec	m	L	f_{MC}
1e-6/15/1	1e-6	15	1	1
1e-4/1/1	1e-4	1	1	1
1e-4/1/50	1e-4	1	50	1
1e-6/15/50	1e-6	15	50	1
1e-4/1/x10	1e-4	1	1	10
1e-5/15/1	1e-5	15	1	1

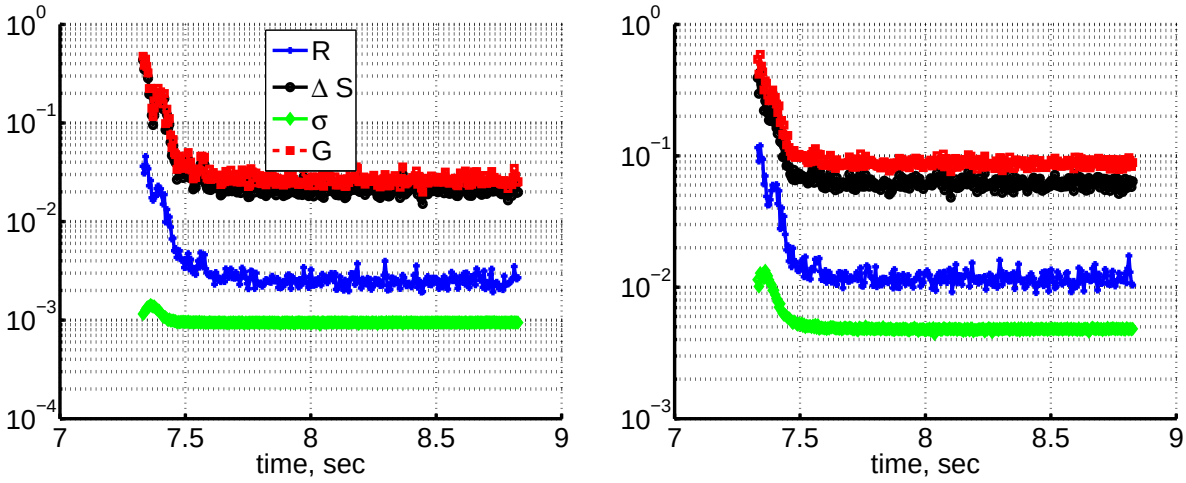

(a) Particle balance

(b) Momentum balance

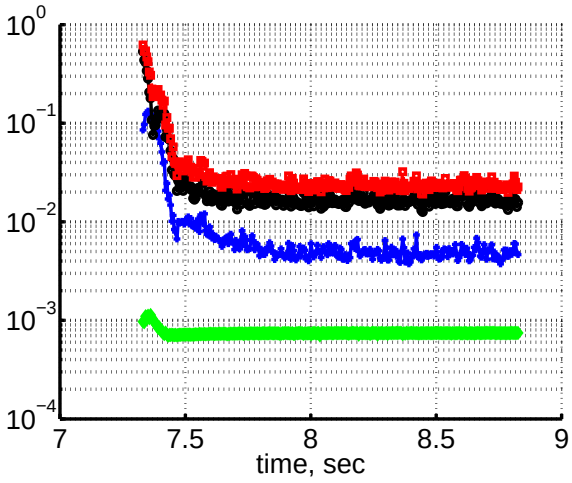

(c) Electron energy balance

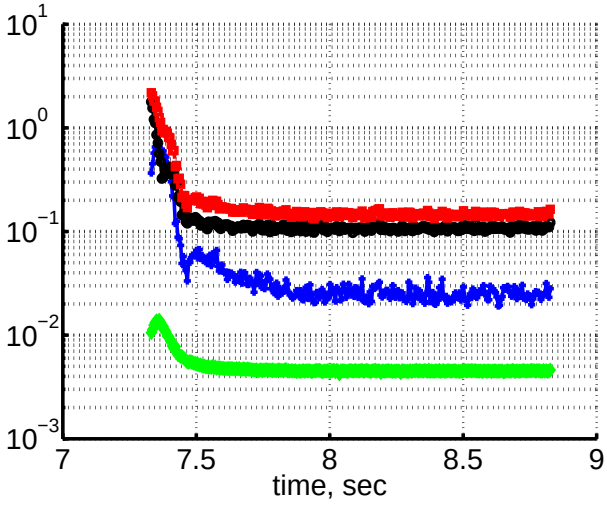

(d) Ion energy balance

Figure 4.1: Time-evolution of *GENRES* ($\hat{G}_\gamma$), model case '1e-4/1/50', see Table 4.1

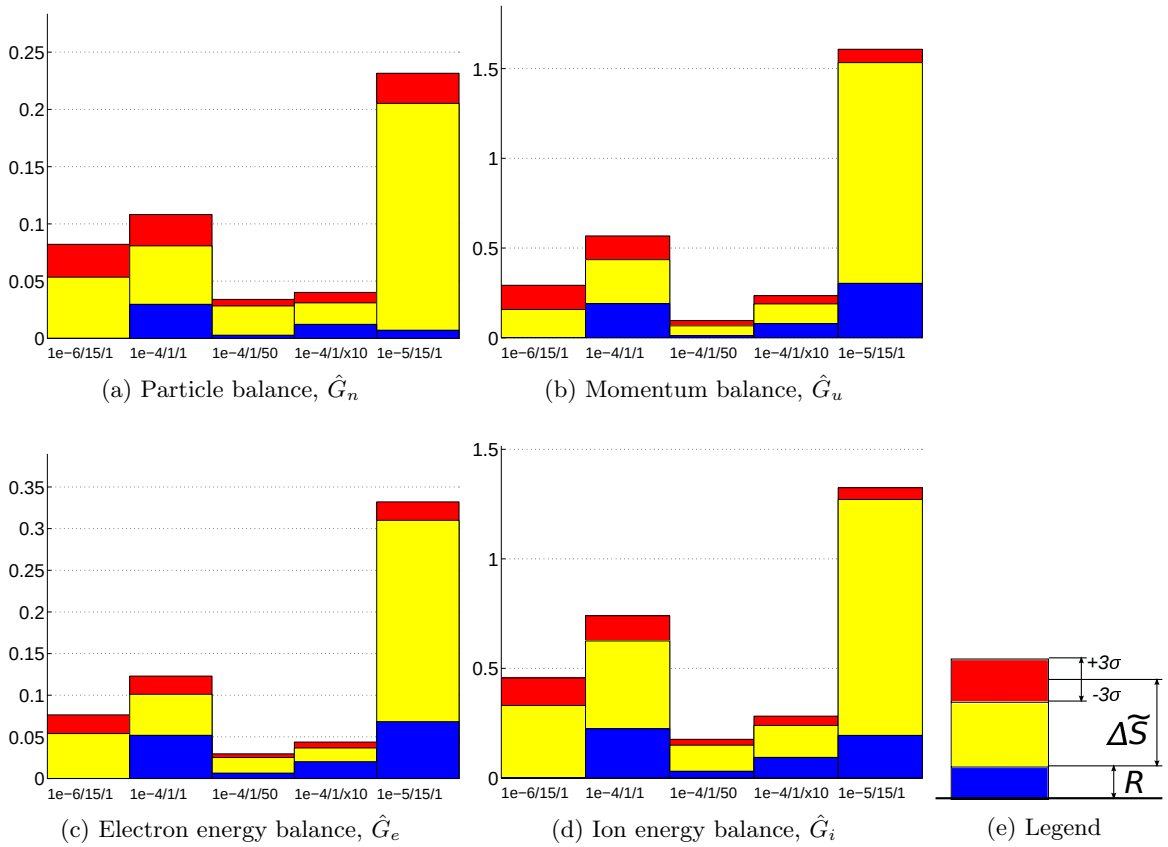

(a) Particle balance, $\hat{G}_n$ (b) Momentum balance, $\hat{G}_u$

(c) Electron energy balance, $\hat{G}_e$ (d) Ion energy balance, $\hat{G}_i$ (e) Legend

Figure 4.2: Normalized generalized residuals, Equation (2.11), for test cases listed in Table 4.1

Table 4.2: Individual terms of *GENRES* for the single fluid test case #2013vk4

case	1e-6/15/1	1e-4/1/1	1e-4/1/50	1e-4/1/x10	1e-5/15/1
$\hat{R}_n$	9.3e-06	3.0e-02	2.8e-03	1.2e-02	7.2e-03
$\Delta\tilde{S}_n$	6.8e-02	6.5e-02	2.8e-02	2.3e-02	2.1e-01
$\hat{\Sigma}_n$	4.6e-02	5.3e-02	1.4e-02	2.2e-02	7.0e-02
$\hat{D}_n$	6.4e-02	8.8e-03	1.2e-03	3.7e-03	1.2e-01
$\hat{\sigma}_n$	4.8e-03	4.6e-03	9.5e-04	1.5e-03	4.4e-03
$\hat{R}_u$	6.4e-05	1.9e-01	1.2e-02	7.9e-02	3.0e-01
$\Delta\tilde{S}_u$	2.3e-01	3.1e-01	6.9e-02	1.3e-01	1.3e+00
$\hat{\Sigma}_u$	2.1e-01	2.3e-01	6.2e-02	7.7e-02	1.8e-01
$\hat{D}_u$	2.1e-01	2.3e-02	2.3e-03	1.0e-02	3.1e-01
$\hat{\sigma}_u$	2.3e-02	2.2e-02	4.9e-03	7.6e-03	1.2e-02
$\hat{R}_e$	5.3e-05	5.2e-02	6.5e-03	2.0e-02	6.8e-02
$\Delta\tilde{S}_e$	6.5e-02	6.0e-02	2.1e-02	2.0e-02	2.5e-01
$\hat{\Sigma}_e$	3.4e-02	3.5e-02	1.1e-02	1.2e-02	5.6e-02
$\hat{D}_e$	4.3e-02	1.0e-02	1.7e-03	3.7e-03	7.6e-02
$\hat{\sigma}_e$	3.7e-03	3.6e-03	7.5e-04	1.2e-03	3.7e-03
$\hat{R}_i$	1.1e-04	2.2e-01	3.1e-02	9.4e-02	1.9e-01
$\Delta\tilde{S}_i$	3.9e-01	4.6e-01	1.3e-01	1.7e-01	1.1e+00
$\hat{\Sigma}_i$	2.8e-01	2.0e-01	9.2e-02	7.4e-02	1.9e-01
$\hat{D}_i$	2.6e-01	7.4e-02	1.2e-02	2.9e-02	2.1e-01
$\hat{\sigma}_i$	2.1e-02	1.9e-02	4.5e-03	7.1e-03	8.9e-03

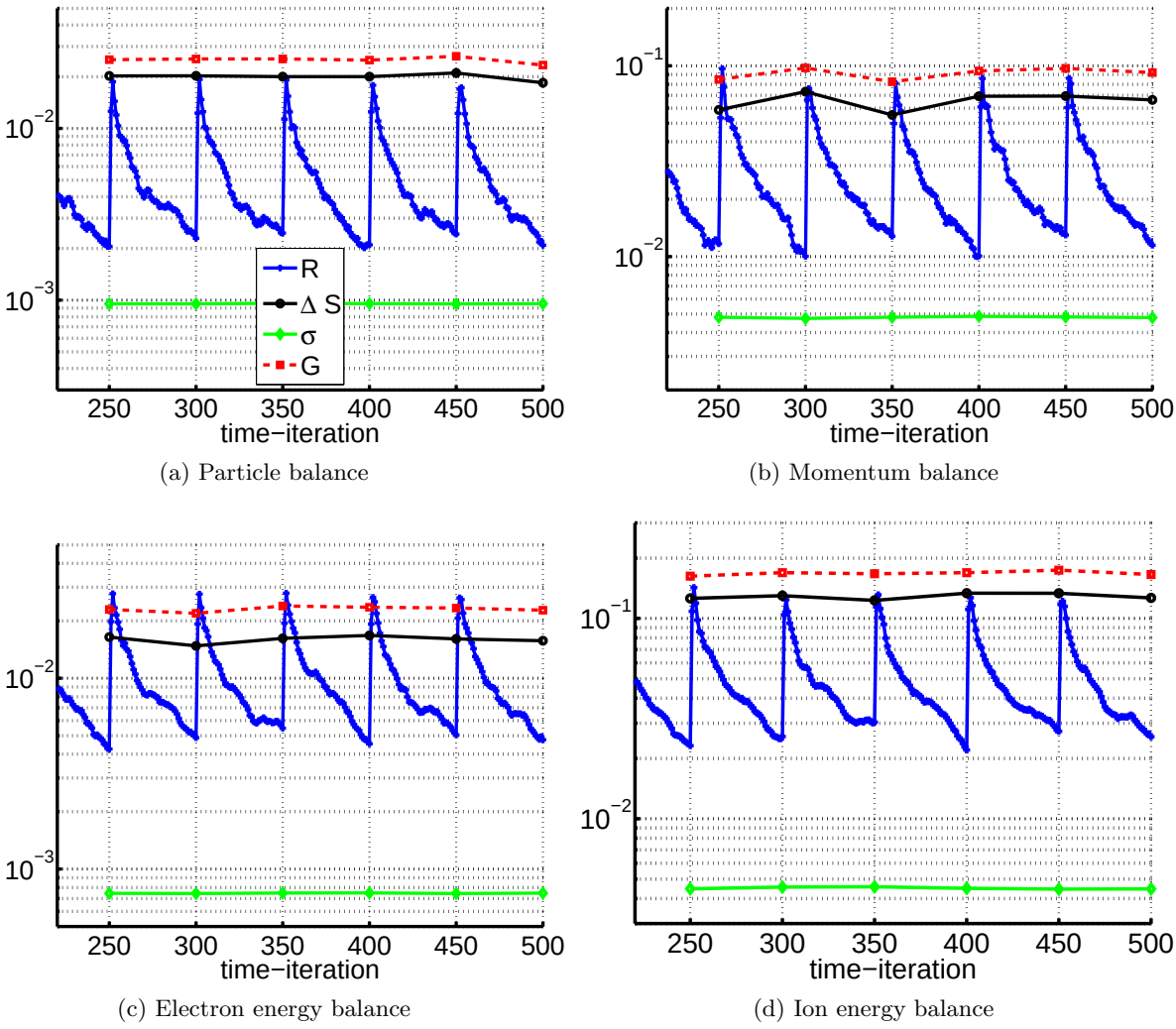

(a) Particle balance

(b) Momentum balance

(c) Electron energy balance

(d) Ion energy balance

Figure 4.3: Normalized residuals $\hat{G}_\gamma$ and their individual terms $\Delta\tilde{S}_\gamma$ and σ_γ, recorded at the end of averaging phases, and (normalized) residuals R_γ, recorded at each time-iteration. Model case '1e-4/1/50', see Table 4.1

time, even very small R does not improve the total error estimate because ΔS stays large.

Test run '1e-5/15/1' is an example of what happens when internal iterations are combined with large Δt. In this case R is not reduced on each time-iteration any more, and the resulting *GENRES* is very large, although formally a steady-state solution is reached.

Solutions obtained using different methods are compared in Figure 4.4. In this figure the parameters in front of divertor targets and on the magnetic separtrix, see Figure 1.1, are shown. Apparently, the solution obtained in the run '1e-5/15/1' significantly deviates from the rest. Such deviation is to be expected since case '1e-5/15/1' has largest *GENRES*. Smaller but visible deviation can be also seen for '1e-4/1/1' which also correlates with the diagram of $\hat{G}_\gamma$, Figure 4.2. The global particle and energy balances of the simulations (see Section 1.3 for definition) are shown in Table 4.3. Error in the energy balance stays on the same level in all tests. Contrary to that, the error in particle balance is significantly larger with $m = 1$ and without averaging (case "1e-4/1/1"), and gets unacceptably large for '1e-5/15/1'.

Since the solutions are close to each other, the diagrams of Figure 4.2 re-plotted in terms of G_α show exactly the same relations between different model runs, with exception of '1e-5/15/1'. Thus, in this case the comparison of normalized values $\hat{G}_\alpha$ is equivalent to comparison of absolute values G_α, and this latter would be more in the sense of Equation (2.4).

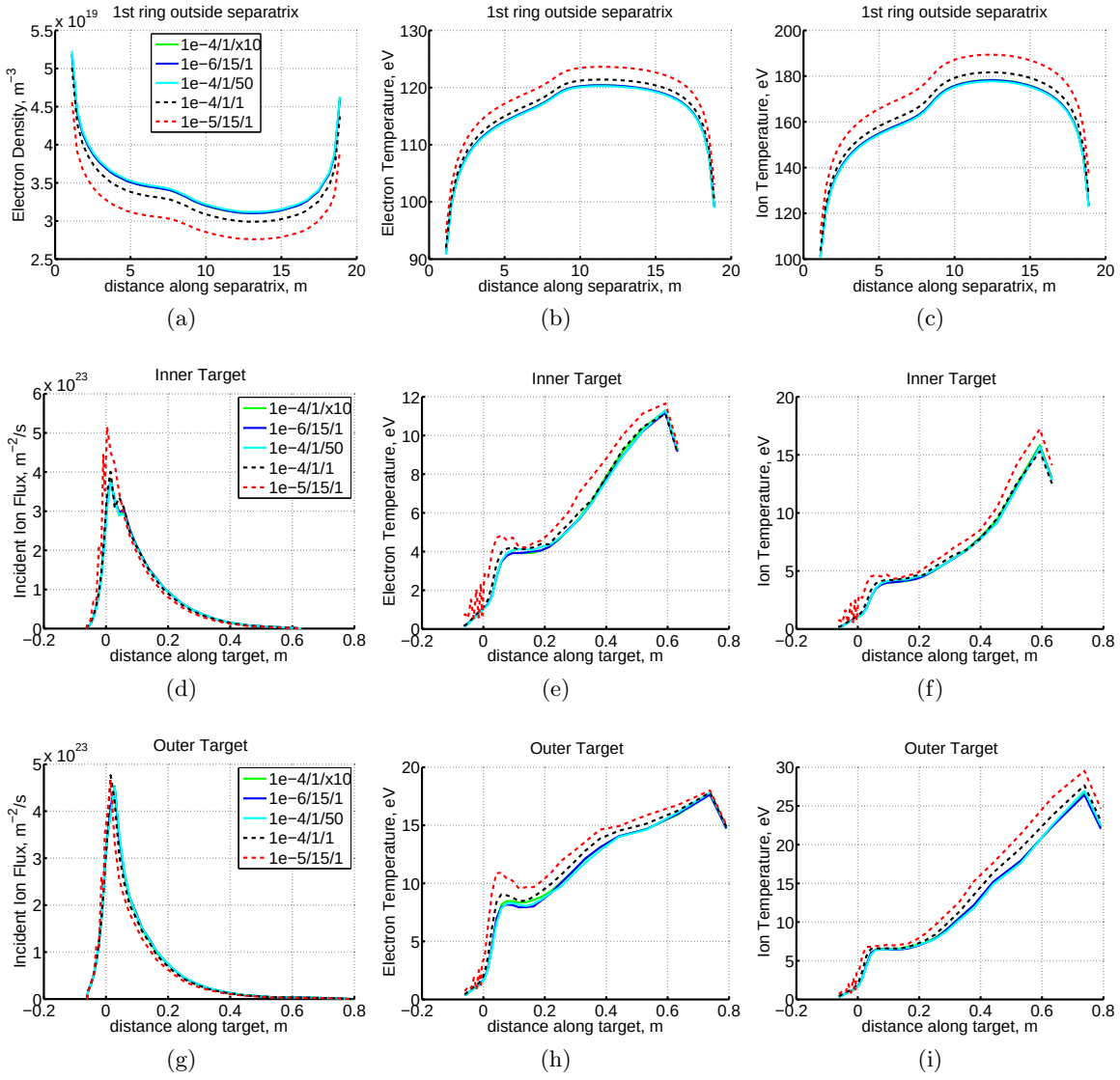

Figure 4.4: Solutions obtained in the test calculations, Table 4.1. Positions of Inner and Outer Targets are shown in Figure 1.1. "Distance along target" is zero at the intersection with magnetic separatrix, positive values point upwards. "Separatrix" is the dashed line in Figure 1.1, "distance along separatrix" goes from inboard to outboard side.

Table 4.3: Particle and energy balance (#2013vk4)

	1e-6/15/1	1e-4/1/1	1e-4/1/50	1e-4/1/x10	1e-5/15/1
$\Delta\Gamma, \%$	2.89	20.92	2.16	2.07	47.95
$\Delta P, \%$	1.49	1.48	1.41	1.41	1.78

Table 4.4: Numerical settings of the multi-fluid test cases (#1568vk4)

Notation	Δt, sec	m	L	f_{MC}
3e-7/20/1	3e-7	20	1	1
5e-5/1/1	5e-5	1	1	1
5e-5/1/50	5e-5	1	50	1
5e-5/1/x40	5e-5	20	1	40

4.2 Multi-fluid test

As a first multi-fluid test the ITER case #1568vk4 was chosen. This is a model with magnetic configuration F57, plasma consisting of electrons and all charged states of D, He and C, and input power P_{SOL}=80 MW. Very low gas puffing rate Γ_{puff}=1.17e22 s^{-1} (p_{PFR}=2 Pa) leads to nearly attached divertor plasma (q_{pk}=8.1 MW/m^2). Under such conditions, it is expected that ion-neutral friction does not play an important role yet. The level of volumetric recombination is low, however, 47 % of P_{SOL} is radiated, mainly due to C. At the same time, low Γ_{puff} makes it challenging to fulfill the particle balance.The standard ITER model is used for the kinetics of neutral particles, including neutral-neutral collisions (and without line radiation transport).

Numerical settings of the test runs are listed in Table 4.4. Characteristic times τ of the runs (defined in Section 1.3) are larger than 3 sec, in particular, τ >10 sec for N_D. For N_{He} τ >10 sec could be reached only for runs '5e-5/1/50' and '5e-5/1/1'. Runs '5e-5/1/50' and '5e-5/1/x40' reached τ of N_{He} of only 4 sec and 3.3 sec respectively, and a visible evolution of the He content still can be observed. This fact is also reflected in the large error in the He particle balance, see Table 4.5. Moreover, it can be seen that the evolution of N_{He} apparently goes in the wrong direction in those two runs: the amount of He ions is decreasing whereas the He flux to the pump is smaller than the influx from the core. Therefore, it did not make sense to try to come close to a stationary state by continuing those runs.

Runs with larger Δt and $m = 20$ were also attempted. It was found that Δt=1e-6 does not lead to divergence of the solution after several thousand time-iterations when started from a stationary state. At the same time, Δt=3e-6 leads to strong increase of residuals and the solution diverges: the error in particle balance gets larger than 90 %. Simulations made with $m = 1$ and larger time step Δt=1e-4 are not discussed here because when time-averaging is applied the solution produced is apparently wrong: violation of the He particle balance and increase of He concentration in front of the divertor targets is so strong that He radiation causes significant perturbation of the solution, whereas normally the He radiated power is insignificant.

Generalized residuals are shown in Figures 4.5, 4.6. It is readily seen that the case with $m = 1$ and $L = 1$ has the largest $\hat{G}$, especially for ion energy and momentum (of the main species). Both averaging and increase of the number of test particles lead to significant suppression of *GENRES*, making them even smaller than in the reference case '3e-7/20/1', with exception of momentum balance for impurities. This latter is always much larger without internal iterations than with $m = 20$, due to increase of the CFD residual R. At the same time, even with m=20 $\hat{G}_u$ for impurities is >1, with ΔS been the dominant error in this case.

Solutions obtained in all four runs are compared in Figure 4.7. Besides large *GENRES*, in the run '5e-5/1/1' also an unacceptably large error in the global particle balance shows up, see Table 4.5. It is not surprising, therefore, that the solution obtained in this run lies far away from other runs - which yield rather close solutions.

From Table 4.5 one can see that in all cases the error in the global energy balance is < 1 %. With $m = 1$ the error in the global particle balance for D is still large: ≈15 % even in the runs with *GENRES* made much smaller than in the reference run '3e-7/20/1', where this error is <2 %. Very large error with $m = 1$ is seen for He as well. In the next section the structure of the error in the global particle balance will be investigated to find an explanation of this result.

Table 4.5: Particle and energy balance (#1568vk4)

	3e-7/20/1	5e-5/1/1	5e-5/1/50	5e-5/1/x40
$\Delta\Gamma_D, \%$	1.39	91.16	14.66	14.35
$\Delta\Gamma_{He}, \%$	6.77	99.41	45.50	54.95
$\Delta P, \%$	0.74	0.45	0.81	0.89

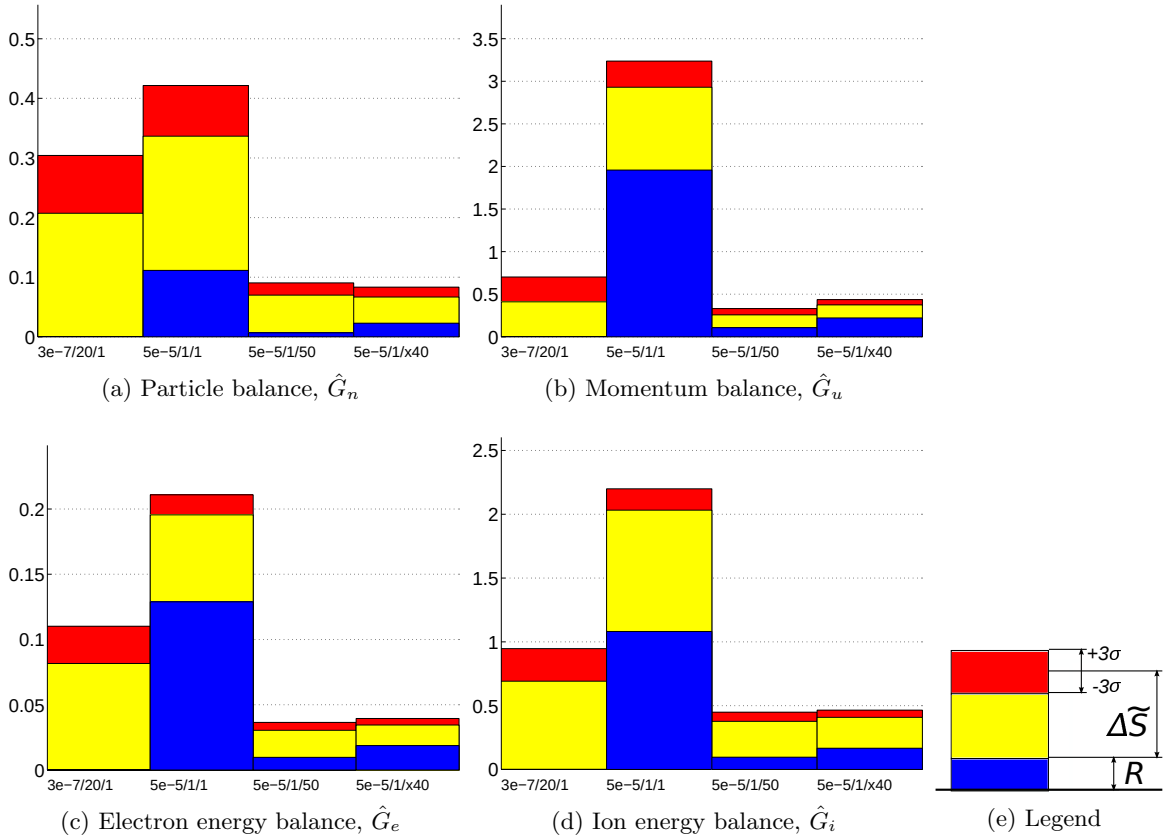

(a) Particle balance, $\hat{G}_n$

(b) Momentum balance, $\hat{G}_u$

(c) Electron energy balance, $\hat{G}_e$

(d) Ion energy balance, $\hat{G}_i$

(e) Legend

Figure 4.5: Normalized generalized residuals, Equation (2.11), for test cases listed in Table 4.4. Particle $\hat{G}_n$ and momentum $\hat{G}_u$ residuals are given for D

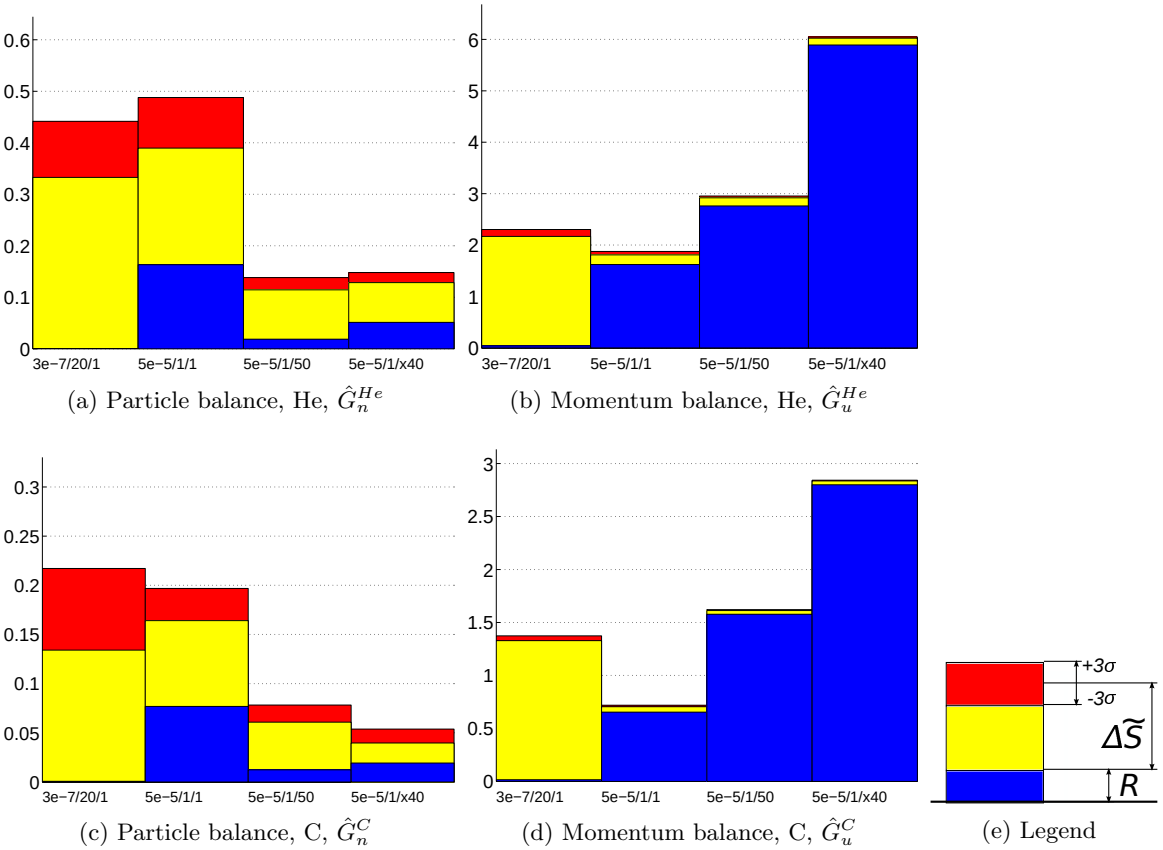

(a) Particle balance, He, $\hat{G}_n^{He}$ (b) Momentum balance, He, $\hat{G}_u^{He}$

(c) Particle balance, C, $\hat{G}_n^{C}$ (d) Momentum balance, C, $\hat{G}_u^{C}$ (e) Legend

Figure 4.6: Normalized generalized residuals, Equation (2.11), for test cases listed in Table 4.4, particle and momentum balance for impurities

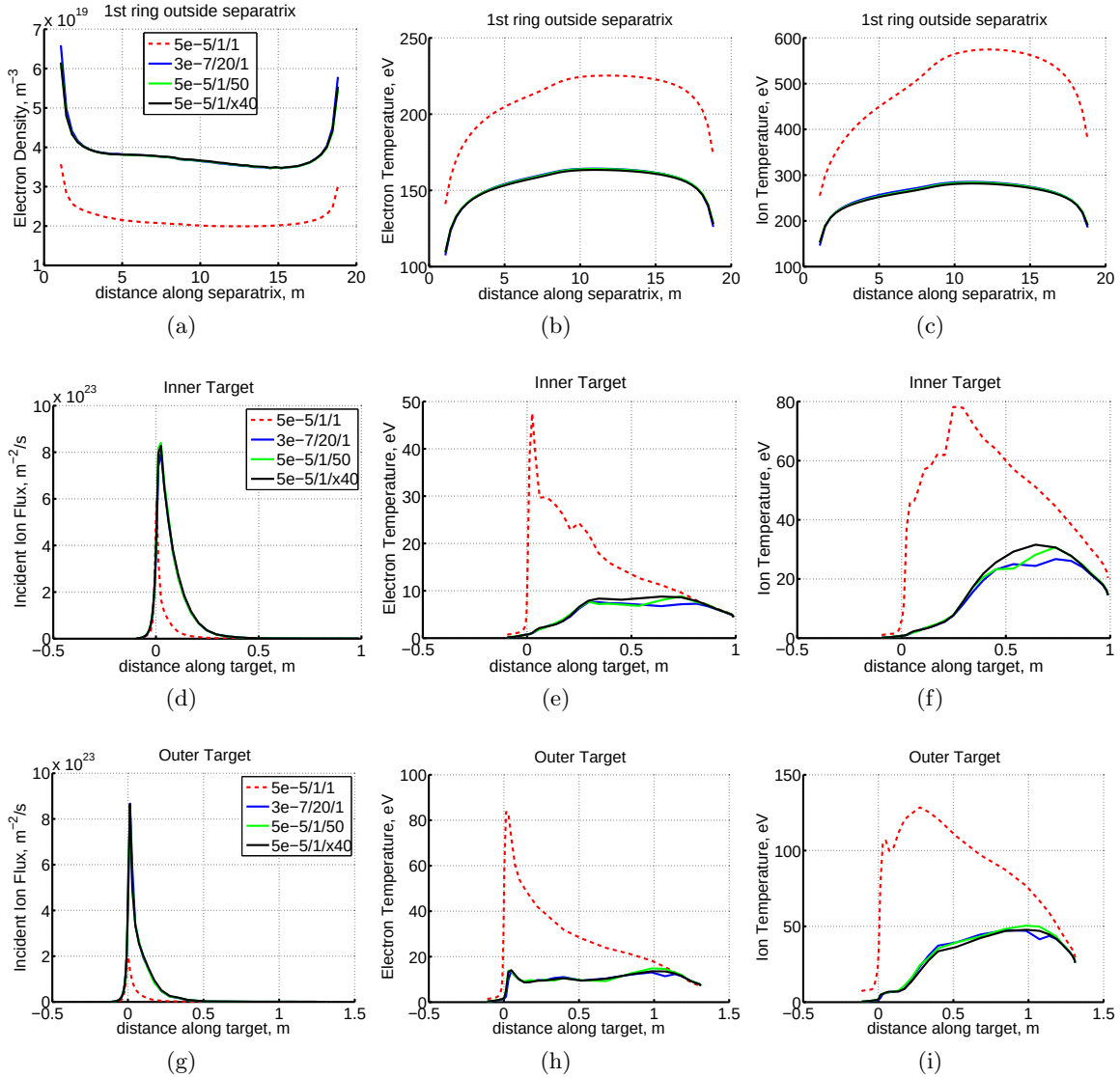

Figure 4.7: Solutions obtained in the multi-fluid test calculations, Table 4.4. Positions of Inner and Outer Targets are shown in Figure 1.1. "Distance along target" is zero at the intersection with magnetic separatrix, positive values point upwards. "Separatrix" is the dashed line in Figure 1.1, "distance along separatrix" goes from inboard to outboard side.

Chapter 5

The particle balance issue

5.1 Diagnostic for particle balance on the CFD side

The expression for the error in the global particle balance for the ion fluid α can be derived in the same way as Equation (2.2) for generalized residual:

$$\hat{R}_n^\alpha = R_n^\alpha(m,k) + \tilde{S}_n^\alpha\left(\phi_k^0|\phi_k^m\right) - \tilde{S}_n^\alpha\left(\phi_k^m\right) + D_n^\alpha\left(\phi_k^m,\phi_k^0\right) \tag{5.1}$$

In this equation, as opposed to Equation (2.2), $\tilde{S}_n^\alpha(\phi_k^m)$ is used instead of $S_n^\alpha(\phi_k^m)$ because the error in the balance shows inconsistency between the actual sources and sinks in the model - independent of the error in the source and sink themselves. The global (integrated) error is then calculated for each ion species β as:

$$E^\beta = \sum_{\alpha'}\sum_i\left(R_n^{\alpha'}(m,k) + \tilde{S}_n^{\alpha'}\left(\phi_k^0|\phi_k^m\right) - \tilde{S}_n^{\alpha'}\left(\phi_k^m\right) + D_n^{\alpha'}\left(\phi_k^m,\phi_k^0\right)\right)$$

Here the sum is taken over all grid cells i and over ion fluids α' which belong to the ion species β: e.g. for the He species these are ion fluids He^+ and He^{++}. The error can be presented as a sum of three terms:

$$E^\beta = E_R^\beta + E_\Delta^\beta + E_T^\beta \tag{5.2}$$

E_R^β is the error due to CFD (B2) residual:

$$E_R^\beta = \sum_{\alpha'}\sum_i R_n^{\alpha'}(m,k)$$

E_Δ^β is the inconsistency of sources at the beginning and at the end of the time-iteration:

$$E_\Delta^\beta = \sum_{\alpha'}\sum_i\left(\tilde{S}_n^{\alpha`}\left(\phi_k^0|\phi_k^m\right) - \tilde{S}_n^{\alpha'}\left(\phi_k^m\right)\right)$$

E_T^β is the time-derivative:

$$E_T^\beta = \sum_{\alpha`}\sum_i D_n^{\alpha`}\left(\phi_k^m,\phi_k^0\right)$$

The time-derivative term E_T^β is, strictly speaking, not an error, but is considered as "error" in the steady-state solution.

Terms of Equation (5.2) are plotted in Figures 5.1 and 5.2 for modelling runs of Section 4.2. 50 last recorded data-points are shown. The new diagnostic, Equation (5.2), is compared to the standard B2 diagnostic based on fluxes, Equation (1.9). This latter contains a slight inconsistency: Γ_{pump} and Γ_{out}^n on the time-iteration k are not taken from the Monte-Carlo run on the background plasma ϕ_k^m. Instead, they are extrapolated from the MC run on plasma ϕ_k^0 using

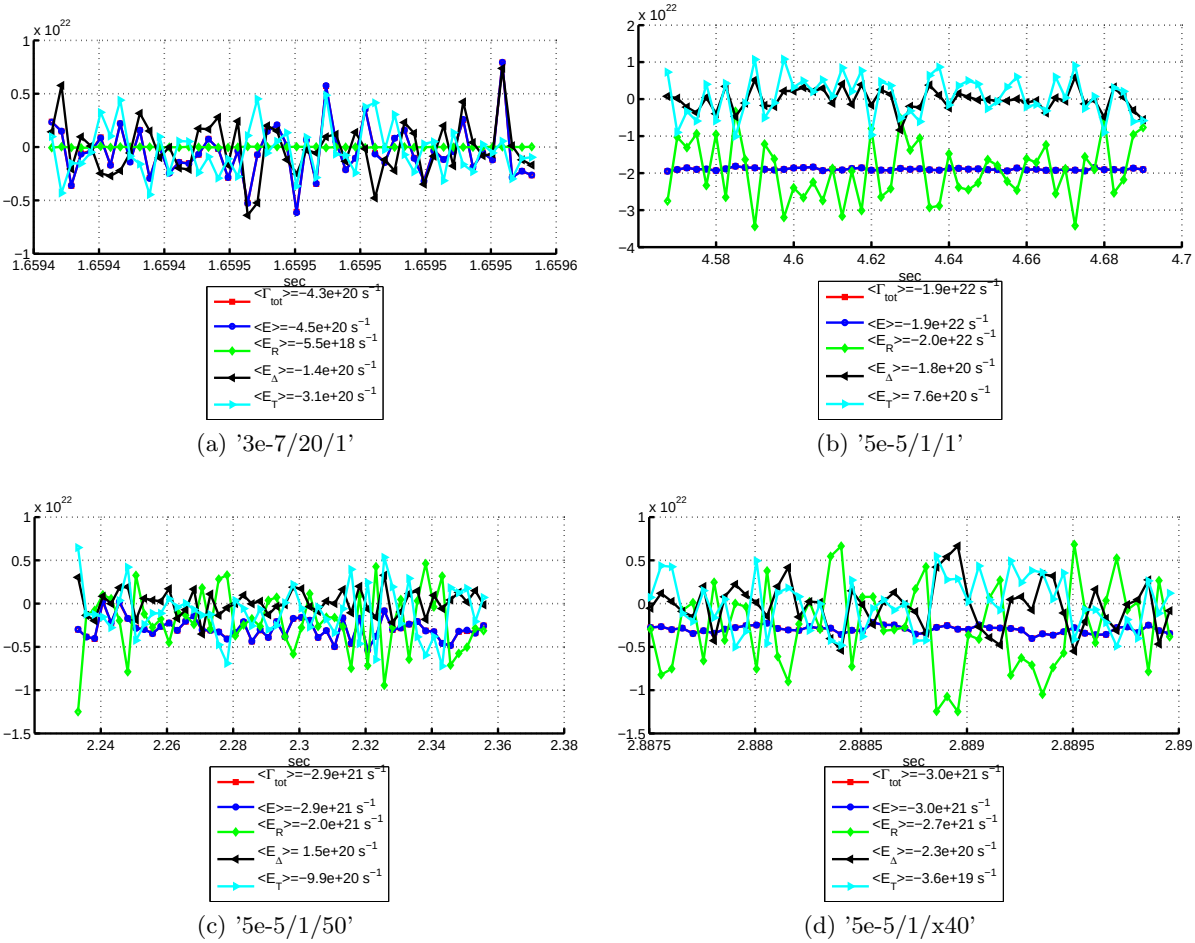

(a) '3e-7/20/1' (b) '5e-5/1/1'

(c) '5e-5/1/50' (d) '5e-5/1/x40'

Figure 5.1: Particle balance for D on the CFD side for four test runs studied in Section 4.2, Table 4.4. E, E_R, E_Δ, E_T are explained in Section 5.1, Equation (5.2). Γ_{tot} is the standard B2 diagnostic, Equation (1.9). $< ... >$ means average over the data points

scaling factors λ_s^β of Equation (1.8). Therefore, there is no exact agreement between those two diagnostics, although the deviation is very small.

Figure 5.1 makes clear the role of internal iterations in reducing the error in the global particle balance. Whereas source inconsistency E_Δ is roughly same in all cases, with $m = 1$ the error is dominated by E_R. Without averaging and increased number of test particles - case '5e-5/1/1' - E_R has the same size as the particle throughput ($\Gamma_{puff} + \Gamma_{in}^+$=2.1e22 s^{-1}). In steady-state the discharge density is controlled by the particle throughput: flux to the pump has to be equal to the throughput, which requires a certain neutral gas pressure in the divertor. The upstream plasma pressure (thus density) is self-adjusted to ensure the required divertor pressure. This self-adjustment mechanism breaks down if the error in the global particle balance is of the order of throughput, and the solution is driven into completely wrong direction. The resulting large discrepancy between solutions can be seen in the previous section, Figure 4.7.

Internal iterations or increased number of Monte-Carlo particles lead to reduction of E_R, but in the tests carried out here with $m = 1$ E_R stays on the level ≈10 % $\left(\Gamma_{puff} + \Gamma_{in}^+\right)$. This is the reason why $\Delta\Gamma_D$ in those cases is larger than in the run '3e-7/20/1', see Table 4.5. The effect is even more pronounced for He, Figure 5.2. The error in the He balance has to be compared with the influx from the core: 2.13e20 s^{-1}. Without internal iterations E_R has similar size even with averaging and increased number of particles. Of note also spikes in E_R seen even with $m = 20$.

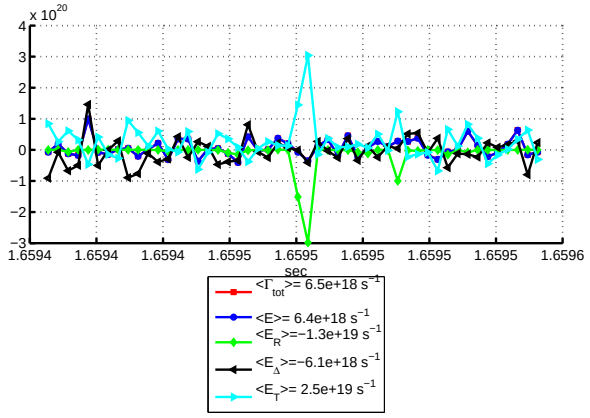

(a) '3e-7/20/1'

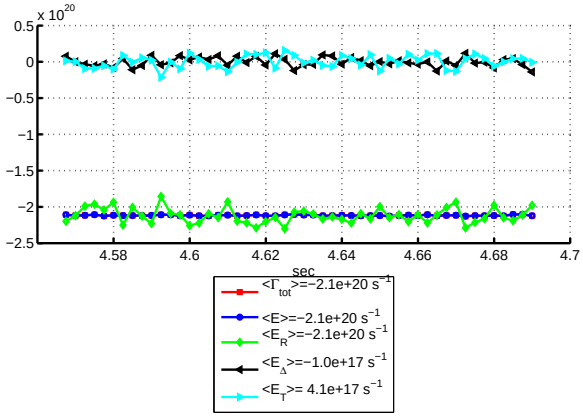

(b) '5e-5/1/1'

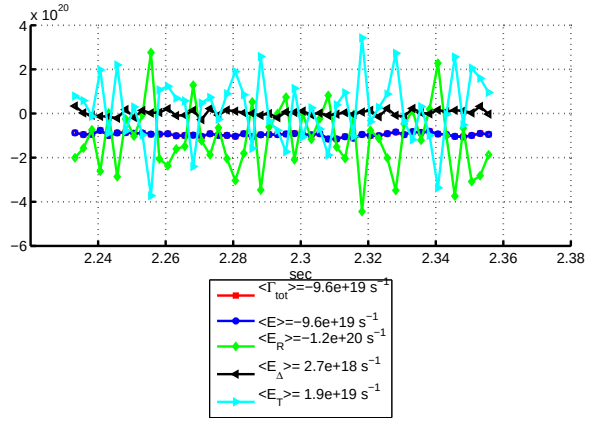

(c) '5e-5/1/50'

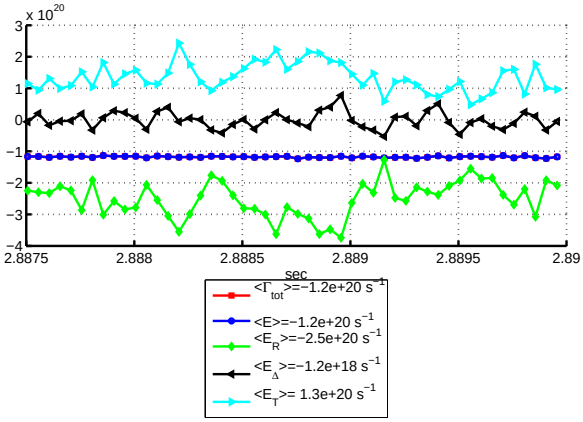

(d) '5e-5/1/x40'

Figure 5.2: Particle balance for He, see caption of Figure 5.1

5.2 Extra iterations for correction of particle balance

To correct the particle balance on the CFD side, the following procedure has been implemented. Instead of Item 9 of the sequences of steps described in Section 1.2, an iterative correction of the particle balance alone is performed. On each iteration $j+1$ the following steps are executed:

1. Calculating source terms and coefficients
2. Defining boundary conditions as sources in guard cells
3. Particle balance, Equation (1.1), for each α:
   $n_\alpha^{j+1} = n_\alpha^j + k\xi$, $u_\alpha^{j+1} = u_\alpha^j - C\frac{\partial \xi}{\partial x}$

The relaxation parameter r for those extra iterations is set to 1. For each species α the following equation for the pressure correction ξ is solved:

$$\frac{1}{\sqrt{g}}\frac{\partial}{\partial x}\frac{\sqrt{g}}{h_x}\left(k\xi u - n_0 C\frac{\partial \xi}{\partial x}\right) + \frac{1}{\sqrt{g}}\frac{\partial}{\partial y}\frac{\sqrt{g}}{h_y}\left(k\xi v^{conv} - kD\frac{\partial \xi}{\partial y}\right) = R =$$
$$= S_n + I - \frac{1}{\sqrt{g}}\frac{\partial}{\partial x}\frac{\sqrt{g}}{h_x}(nu) - \frac{1}{\sqrt{g}}\frac{\partial}{\partial y}\frac{\sqrt{g}}{h_y}\left(nv^{conv} - D\frac{\partial n}{\partial y}\right) \tag{5.3}$$

Here $k = \frac{1}{ZT_e+T_i}$, u is the poloidal velocity found from Equation (1.2), D is the diffusion coefficient, v is the radial convection velocity, C is the pressure correction factor. For simplicity, the subscript α is omitted in Equation (5.3) and below. Modification of velocity, $u_\alpha^{j+1} = u_\alpha^j - C\frac{\partial \xi}{\partial x}$, is kept in the correction scheme because otherwise the overall solution was found to become unstable.

Equation (5.3) is linear with respect to ξ, however, an iterative procedure is required due to several reasons. First, the term I - particle source due to ionization and recombination of ions - is a non-linear function of ion density. Second, for the term S_n the re-scaling with incident ion fluxes, Equation (1.8), is applied. Strictly speaking, this re-scaling does not introduce non-linearity because fluxes are proportional to the ion densities, but in practice the source terms are fixed when the set of linear equations for ξ (see below) is solved, and the re-calculation of sources is taken into account in an iterative way. In addition to that, finite volume discretization of the continuity equation in B2 is based on the hybrid upwind scheme, see [7], Equation (12). This scheme allows higher order of (spatial) approximation than pure upwind, but leads to non-linear dependency of the coefficients of finite-volume equations for the density. To remove this extra non-linearity and, thus, to increase the chance for iterations to converge, the finite-volume scheme has been downgraded to pure upwind.

For completeness, the discretization of the continuity equation and its boundary condition - as it was applied in all simulations of the present report - is described below. The upwind scheme for Equation (5.3) reads as follows, see Figure 5.3a:

$$flox_{ix,iy} \cdot \begin{cases} \xi_{ix,iy}, & flox_{ix,iy} \geq 0 \\ \xi_{ix+1,iy}, & flox_{ix,iy} < 0 \end{cases} - flox_{ix-1,iy} \cdot \begin{cases} \xi_{ix-1,iy}, & flox_{ix-1,iy} \geq 0 \\ \xi_{ix,iy}, & flox_{ix-1,iy} < 0 \end{cases} +$$
$$+ floy_{ix,iy} \cdot \begin{cases} \xi_{ix,iy}, & floy_{ix,iy} \geq 0 \\ \xi_{ix,iy+1}, & floy_{ix,iy} < 0 \end{cases} - floy_{ix,iy-1} \cdot \begin{cases} \xi_{ix,iy-1}, & floy_{ix,iy-1} \geq 0 \\ \xi_{ix,iy}, & floy_{ix,iy-1} < 0 \end{cases} -$$
$$- conx_{ix,iy} \cdot (\xi_{ix+1,iy} - \xi_{ix,iy}) + conx_{ix-1,iy} \cdot (\xi_{ix,iy} - \xi_{ix-1,iy}) -$$
$$- cony_{ix,iy} \cdot (\xi_{ix+1,iy} - \xi_{ix,iy}) + cony_{ix,iy-1} \cdot (\xi_{ix,iy} - \xi_{ix,iy-1}) -$$
$$- S^v_{ix,iy} k_{ix,iy} \xi_{ix,iy} = res_{ix,iy} \tag{5.4}$$

$$res_{ix,iy} = S^c_{ix,iy} + S^v_{ix,iy} n_{ix,iy} - fnix_{ix,iy} + fnix_{ix-1,iy} - fniy_{ix,iy} + fniy_{ix,iy-1} \tag{5.5}$$

Here:

$$flox_{ix,iy} = u_{ix,iy} \cdot s^x_{ix,iy} \cdot \begin{cases} k_{ix,iy}, & u_{ix,iy} \geq 0 \\ k_{ix+1,iy}, & u_{ix,iy} < 0 \end{cases}$$

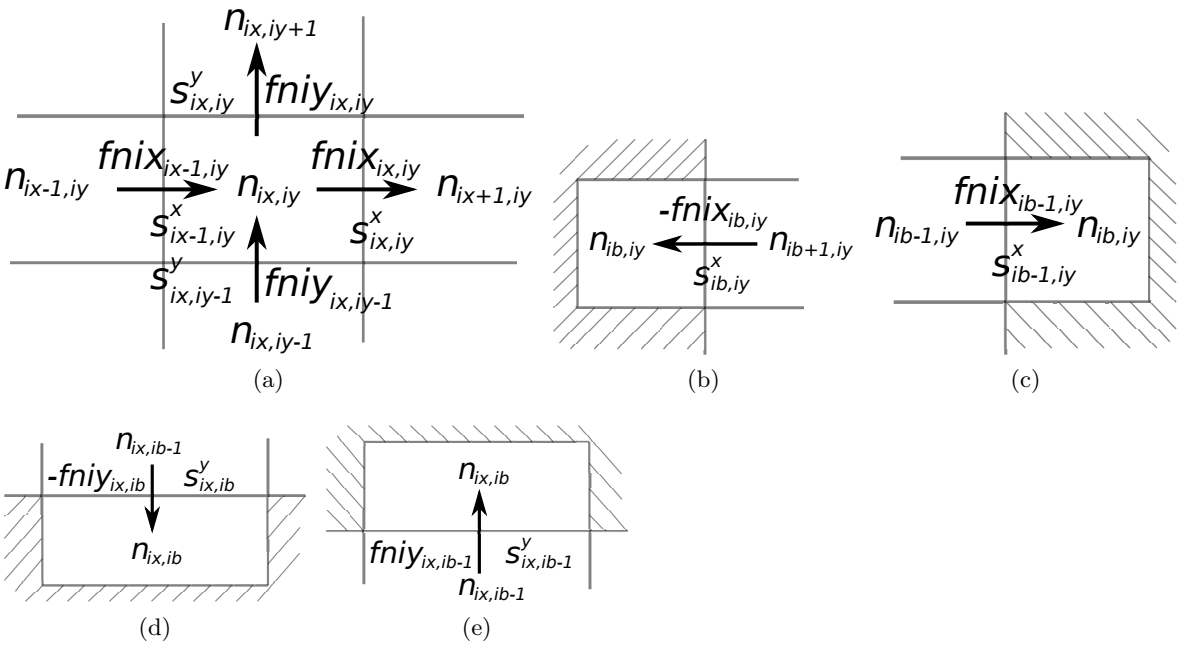

Figure 5.3: Sketches of the finite-volume scheme for the continuity equation. Density n is defined in cell centers. Fluxes, as well as velocities, are defined at cell faces.

$$floy_{ix,iy} = v^{conv}_{ix,iy} \cdot s^y_{ix,iy} \cdot \begin{cases} k_{ix,iy}, & v^{conv}_{ix,iy} \geq 0 \\ k_{ix,iy+1}, & v^{conv}_{ix,iy} < 0 \end{cases}$$

$$conx_{ix,iy} = C_{ix,iy} \cdot s^x_{ix,iy}, \quad cony_{ix,iy} = \frac{2\bar{D}_{ix,iy}}{\left(\Delta^y_{ix,iy} + \Delta^y_{ix,iy+1}\right)\bar{T}_{ix,iy}} \cdot s^x_{ix,iy}$$

$$\bar{T}_{ix,iy} = 0.5 \cdot \left(T_i^{ix,iy} + Z \cdot T_e^{ix,iy} + T_i^{ix,iy+1} + Z \cdot T_e^{ix,iy+1}\right)$$

$$\bar{D}_{ix,iy} = \frac{D_{ix,iy} \cdot \Delta^y_{ix,iy} + D_{ix,iy+1} \cdot \Delta^y_{ix,iy+1}}{\Delta^y_{ix,iy} + \Delta^y_{ix,iy+1}}$$

$$fnix_{ix,iy} = u_{ix,iy} \cdot s^x_{ix,iy} \cdot \begin{cases} n_{ix,iy}, & u_{ix,iy} \geq 0 \\ n_{ix+1,iy}, & u_{ix,iy} < 0 \end{cases} \tag{5.6}$$

$$fniy_{ix,iy} = cony_{ix,iy} \cdot \bar{T}_{ix,iy} \cdot (n_{ix,iy+1} - n_{ix,iy}) + v^{conv}_{ix,iy} \cdot s^y_{ix,iy} \cdot \begin{cases} n_{ix,iy}, & v^{conv}_{ix,iy} \geq 0 \\ n_{ix,iy+1}, & v^{conv}_{ix,iy} < 0 \end{cases} \tag{5.7}$$

Here s^x and s^y are areas of the cell faces, Δ^y is the radial grid step. Superscript j is omitted. Source linearization is applied for the particle source $\tilde{S}_n$:

$$\tilde{S}_n^{ix,iy} + I^{ix,iy} = S^c_{ix,iy} + S^v_{ix,iy} \cdot n_{ix,iy}$$

$$S^c_{ix,iy} = I^{ix,iy} + \begin{cases} \tilde{S}_n^{ix,iy}, & S_n^{ix,iy} > 0 \\ 0, & S_n^{ix,iy} \leq 0 \end{cases} + r_f \left|\tilde{S}_n^{ix,iy}\right| + \frac{n^0_{ix,iy} \cdot vol_{ix,iy}}{\Delta t}$$

$$S^v_{ix,iy} = \begin{cases} 0, & \tilde{S}_n^{ix,iy} > 0 \\ \tilde{S}_n^{ix,iy}, & \tilde{S}_n^{ix,iy} \leq 0 \end{cases} - r_f \frac{\left|\tilde{S}_n^{ix,iy}\right|}{n_{ix,iy}} - \frac{vol_{ix,iy}}{\Delta t},$$

Here vol is the cell volume. In all calculations here the parameter $r_f > 0$ is set to 5. $S^c \geq 0$ and $S^v < 0$ is mandatory for numerical stability, see [10], Chapter 7.2.

Boundary conditions in B2 are defined through defining sources in the boundary (guard) cells such that residual, Equation (5.5), equals to zero there. It is assumed that there is no

flux between guard cells and that there is no flux across the free boundary. Only boundary conditions which were used in the present tests are described below.

On the divertor targets the boundary condition $\frac{\partial n}{\partial x} = 0$ is used. On the west (inner) target this condition translates into $n_{ib,iy} = n_{ib+1,iy}$, see Figure 5.3b, and $fnix_{ib-1,iy} = 0$, $fniy = 0$, $u_{ib,iy} \leq 0$ yields:

$$res_{ib,iy} = S^c_{ib,iy} + S^v_{ib,iy} n_{ib,iy} - u_{ib,iy} s^x_{ib,iy} n_{ib+1,iy} = 0 \Rightarrow S^c_{ib,iy} = 0,\ S^v_{ib,iy} = u_{ib,iy} s^x_{ib,iy} \tag{5.8}$$

Similar for the east (outer) target, Figure 5.3c: $n_{ib,iy} = n_{ib-1,iy}$, $fnix_{ib,iy} = 0$, $fniy = 0$, $u_{ib,iy} \geq 0$, thus:

$$\begin{gathered} res_{ib,iy} = S^c_{ib,iy} + S^v_{ib,iy} n_{ib,iy} + u_{ib-1,iy} s^x_{ib-1,iy} n_{ib-1,iy} = 0 \Rightarrow \\ S^c_{ib,iy} = 0,\ S^v_{ib,iy} = -u_{ib-1,iy} s^x_{ib-1,iy} \end{gathered} \tag{5.9}$$

On the poloidal surfaces the radial decay length is prescribed: $l^{-1} = \frac{1}{n}\frac{\partial n}{\partial x}$, $\frac{\partial n}{\partial y} > 0$ or $l^{-1} = -\frac{1}{n}\frac{\partial n}{\partial x}$, $\frac{\partial n}{\partial y} < 0$. In pure diffusion approximation the radial flux density at the guard cell is then translated to: $\Gamma_r = -D\frac{\partial n}{\partial y} = \mp\frac{Dn}{l}$. Therefore, for the south (PFR - private flux region) boundary, Figure 5.3d, one can write $fniy_{ix,ib} = -\frac{\bar{D}_{ix,ib}}{l_{ib}} s^y_{ix,ib} n_{iy,ib}$ ($\frac{\partial n}{\partial y} > 0$), $fniy_{ix,ib-1} = 0$, $fnix = 0$ and:

$$res_{ix,ib} = S^c_{ix,ib} + S^v_{ix,iy} n_{ix,ib} + \frac{\bar{D}_{ix,ib}}{l_{ib}} s^y_{ix,ib} n_{iy,ib} = 0 \Rightarrow S^c_{ix,ib} = 0, \quad S^v_{ix,ib} = -\frac{\bar{D}_{ix,ib}}{l_{ib}} s^y_{ix,ib}$$

Similar, for the north (main chamber wall) boundary, Figure 5.3e, $fniy_{ix,ib-1} = \frac{\bar{D}_{ix,ib-1}}{l_{ib}} s^y_{ix,ib-1} n_{iy,ib}$ ($\frac{\partial n}{\partial y} < 0$), $fniy_{ix,ib} = 0$, $fnix = 0$:

$$res_{ix,ib} = S^c_{ix,ib} + S^v_{ix,iy} n_{ix,ib} + \frac{\bar{D}_{ix,ib-1}}{l_{ib}} s^y_{ix,ib-1} n_{iy,ib} = 0 \Rightarrow S^c_{ix,ib} = 0, \quad S^v_{ix,ib} = -\frac{\bar{D}_{ix,ib-1}}{l_{ib}} s^y_{ix,ib-1}$$

Finally, the constant flux density boundary condition on the south boundary is specified as follows: $fniy_{ix,ib} = f_{in} s^y_{ib}$, $fniy_{ix,ib-1} = 0$, $fnix = 0$, where f_{in} is the prescribed flux density. Therefore:

$$res_{ix,ib} = S^c_{ix,ib} + S^v_{ix,iy} n_{ix,ib} - f_{in} s^y_{ix,ib} = 0 \Rightarrow S^c_{ix,ib} = f_{in} s^y_{ix,ib}, \quad S^v_{ix,ib} = 0$$

In summary, the following changes have been implemented in the B2 code in order to make the extra particle balance iterations - "continuity iterations" - reliable:

1. Pure upwind scheme, Equation (5.4), instead of modified upwind scheme

2. Boundary conditions in the form of Equations (5.8), (5.9), instead of the explicit implementation used originally: $n^j_{ib} = n^{j-1}_{ib+1}$ (west), $n^j_{ib} = n^{j-1}_{ib-1}$ (east)

3. Diffusive part of the radial velocity is treated implicitly in Equation (5.4) instead of including it into pre-calculated v^{conv}

4. A bug is fixed in the calculations of the coefficients of 5-point equations which are sent to the matrix sparse solver

The modifications listed above were switched on in all calculations described in the present report. In addition, the tolerance parameter of the matrix sparse solver was set 0.

5.3 Testing the correction scheme

It is to be expected that when Equation (5.4) is solved, the correction $n_\alpha^{j+1} = n_\alpha^j + k\xi$ is made and fluxes, Equations (5.6) and (5.7), are calculated, then the residual, Equation (5.5), has to drop immediately to a very small value determined only by round-off error (machine precision). Two extra options had to be implemented in the code to execute this test:

1. Fluxes and residual are calculated right after solution of Equation (5.4)
2. Calculation of velocity correction, $u_\alpha^{j+1} = u_\alpha^j - C\frac{\partial\xi}{\partial x}$, is modified to yield exactly the updated flux

The first item is required because normally B2 calculates residuals only before solution of equations. That means that even if after solution of Equation (5.4) the balance was exact, still a large residual can be detected because the source-terms are re-calculated, in particular, S_n is re-scaled, Equation (1.8).

Expression for the term $-C\frac{\partial\xi}{\partial x} = \Delta u_{ix,iy}$ which leads to exact fulfillment of Equation (5.5) is found from the condition:

$$fnix_{ix,iy} + flox_{ix,iy} \cdot \begin{cases} \xi_{ix,iy}, & flox_{ix,iy} \geq 0 \\ \xi_{ix+1,iy}, & flox_{ix,iy} < 0 \end{cases} - conx_{ix,iy} \cdot (\xi_{ix+1,iy} - \xi_{ix,iy}) = fnix_{ix,iy}^{j+1} \quad (5.10)$$

Here the superscript j for the old values is omitted, $conx_{ix,iy} = C_{ix,iy} \cdot s_{ix,iy}^x$. Four special cases have to be considered.

Case 1: $u_{ix,iy}^j \geq 0$, $u_{ix,iy}^{j+1} \geq 0$. Thus, $fnix_{ix,iy} = u_{ix,iy} \cdot s_{ix,iy}^x \cdot n_{ix,iy}$, $flox_{ix,iy} = u_{ix,iy} \cdot s_{ix,iy}^x \cdot k_{ix,iy}$, $fnix_{ix,iy}^{j+1} = (u_{ix,iy} + \Delta u_{ix,iy})\, s_{ix,iy}^x\, (n_{ix,iy} + k_{ix,iy}\xi_{ix,iy})$. Equation (5.10) then reads:

$$u_{ix,iy} \cdot s_{ix,iy}^x \cdot n_{ix,iy} + u_{ix,iy} \cdot s_{ix,iy}^x \cdot k_{ix,iy} \cdot \xi_{ix,iy} - C_{ix,iy} \cdot s_{ix,iy}^x\, (\xi_{ix+1,iy} - \xi_{ix,iy}) =$$
$$(u_{ix,iy} + \Delta u_{ix,iy})\, s_{ix,iy}^x\, (n_{ix,iy} + k_{ix,iy}\xi_{ix,iy}) \Rightarrow \Delta u_{ix,iy} = -\frac{C_{ix,iy}\, (\xi_{ix+1,iy} - \xi_{ix,iy})}{n_{ix,iy} + k_{ix,iy}\xi_{ix,iy}}$$

Therefore:

$$u_{ix,iy}^{j+1} = u_{ix,iy}^j - \frac{C_{ix,iy}\, (\xi_{ix+1,iy} - \xi_{ix,iy})}{n_{ix,iy}^{j+1}} \quad (5.11)$$

Case 2: $u_{ix,iy}^j \geq 0$, $u_{ix,iy}^{j+1} < 0$. Thus, $fnix_{ix,iy}^{j+1} = (u_{ix,iy} + \Delta u_{ix,iy})\, s_{ix,iy}^x\, (n_{ix+1,iy} + k_{ix+1,iy}\xi_{ix+1,iy})$ and:

$$u_{ix,iy} \cdot s_{ix,iy}^x \cdot n_{ix,iy} + u_{ix,iy} \cdot s_{ix,iy}^x \cdot k_{ix,iy} \cdot \xi_{ix,iy} - C_{ix,iy} \cdot s_{ix,iy}^x\, (\xi_{ix+1,iy} - \xi_{ix,iy}) =$$
$$(u_{ix,iy} + \Delta u_{ix,iy})\, s_{ix,iy}^x\, (n_{ix+1,iy} + k_{ix+1,iy}\xi_{ix+1,iy})$$

Therefore:

$$u_{ix,iy}^{j+1} = \frac{u_{ix,iy} \cdot n_{ix,iy}^{j+1} - C_{ix,iy}\, (\xi_{ix+1,iy} - \xi_{ix,iy})}{n_{ix+1,iy}^{j+1}} = \frac{n_{ix,iy}^{j+1}}{n_{ix+1,iy}^{j+1}} \left(u_{ix,iy}^j - \frac{C_{ix,iy}\, (\xi_{ix+1,iy} - \xi_{ix,iy})}{n_{ix,iy}^{j+1}} \right) \quad (5.12)$$

From Equations (5.11), (5.12) it is readily seen that if $u_{ix,iy}^j \geq 0$ then $u_{ix,iy}^{j+1}$ can be calculated as follows. First Equation (5.11) is applied. If resulting $u_{ix,iy}^{j+1} \geq 0$ then the initial assumption was correct. Otherwise, $u_{ix,iy}^{j+1}$ is multiplied by $\frac{n_{ix,iy}^{j+1}}{n_{ix+1,iy}^{j+1}} > 0$. Since this multiplication does not change the sign the assumption of Equation (5.12) holds.

Similar for $u_{ix,iy}^j < 0$. Case 3, $u_{ix,iy}^j < 0$, $u_{ix,iy}^{j+1} < 0$, thus, $fnix_{ix,iy} = u_{ix,iy} \cdot s_{ix,iy}^x \cdot n_{ix+1,iy}$, $flox_{ix,iy} = u_{ix,iy} \cdot s_{ix,iy}^x \cdot k_{ix+1,iy}$, $fnix_{ix,iy}^{j+1} = (u_{ix,iy} + \Delta u_{ix,iy})\, s_{ix,iy}^x\, (n_{ix+1,iy} + k_{ix+1,iy}\xi_{ix+1,iy})$, Equation (5.10):

$$u_{ix,iy} \cdot s_{ix,iy}^x \cdot n_{ix+1,iy} + u_{ix,iy} \cdot s_{ix,iy}^x \cdot k_{ix+1,iy} \cdot \xi_{ix+1,iy} - C_{ix,iy} \cdot s_{ix,iy}^x\, (\xi_{ix+1,iy} - \xi_{ix,iy}) =$$
$$= (u_{ix,iy} + \Delta u_{ix,iy})\, s_{ix,iy}^x\, (n_{ix+1,iy} + k_{ix+1,iy}\xi_{ix+1,iy})$$

Therefore:

$$u^{j+1}_{ix,iy} = u_{ix,iy} - \frac{C_{ix,iy}\left(\xi_{ix+1,iy} - \xi_{ix,iy}\right)}{n^{j+1}_{ix+1,iy}} \tag{5.13}$$

Case 4, $u^{j}_{ix,iy} < 0$, $u^{j+1}_{ix,iy} \geq 0$, thus, $fnix^{j+1}_{ix,iy} = \left(u_{ix,iy} + \Delta u_{ix,iy}\right) s^{x}_{ix,iy}\left(n_{ix,iy} + k_{ix,iy}\xi_{ix,iy}\right)$ and:

$$u_{ix,iy} \cdot s^{x}_{ix,iy} \cdot n_{ix+1,iy} + u_{ix,iy} \cdot s^{x}_{ix,iy} \cdot k_{ix+1,iy} \cdot \xi_{ix+1,iy} - C_{ix,iy} \cdot s^{x}_{ix,iy}\left(\xi_{ix+1,iy} - \xi_{ix,iy}\right) =$$
$$= \left(u_{ix,iy} + \Delta u_{ix,iy}\right) s^{x}_{ix,iy}\left(n_{ix,iy} + k_{ix,iy}\xi_{ix,iy}\right)$$

Therefore:

$$u^{j+1}_{ix,iy} = \frac{n^{j+1}_{ix+1,iy}}{n^{j+1}_{ix,iy}}\left(u_{ix,iy} - \frac{C_{ix,iy}\left(\xi_{ix+1,iy} - \xi_{ix,iy}\right)}{n^{j+1}_{ix+1,iy}}\right) \tag{5.14}$$

Finally, if $u^{j}_{ix,iy} < 0$ then $u^{j+1}_{ix,iy}$ is first calculated using Equation (5.13), and if it turns out to be larger than zero, then $u^{j+1}_{ix,iy}$ is multiplied by $\frac{n^{j+1}_{ix+1,iy}}{n^{j+1}_{ix,iy}}$.

It is found that the velocity correction described by Equations (5.11), (5.14) can lead to instability. Therefore, this correction is used only for test purposes. In the regular runs the following approximation is applied (B2 original):

$$u^{j+1}_{ix,iy} = u_{ix,iy} - \frac{C_{ix,iy}\left(\xi_{ix+1,iy} - \xi_{ix,iy}\right)}{0.5\left(n^{j+1}_{ix+1,iy} + n^{j+1}_{ix,iy} + \max\left(\left|k_{ix,iy}\xi_{ix,iy}\right|, \left|k_{ix+1,iy}\xi_{ix+1,iy}\right|\right) + 10^{-60}\right)}$$

Results of the test runs performed for the ITER case #1568vk4 (see Section 4.2) are presented in Figure 5.4 where the behavior of the residuals of continuity equations is shown. D^{+} and He^{+} ions are taken as an example, other ion fluids demonstrate similar behavior. The residuals are calculated right after solution of Equation (5.4) and presented in the form standard to B2 ,that is , normalized by the total amount of ions. Velocity correction is calculated in the form described above. One full internal iteration, and 9 extra continuity iterations, as described in Section 5.2, are executed. Very small time-step Δt=1e-8 sec is taken in order to make sure that no problem with negative sources can appear, see Section 5.4.

On the first time-iteration (first 10 iterations) the continuity equations are solved as originally implemented in B2. Then, the bug fix in the calculation of five-point coefficients is switched on. On the third time-iteration the bug fix is switched off, but the modified upwind scheme is replaced by pure upwind. This latter also includes implicit implementation of the radial diffusion term and boundary condition at the divertor targets, items 1, 2, 3 in Section 5.2. On the last time-iteration both corrections are switched on. As expected, in this last case the residual drops to its minimal value immediately after the first correction of the continuity equation.

5.4 Potential problem with too strong negative sources

A too strong negative particle source - volumetric recombination - can potentially lead to a situation when all ions are removed from a cell during one time-iteration and the density formally gets negative. To prevent negative densities, corrections ξ which emerge after solution of Equation (5.4) are artificially restricted from below:

$$\xi_{ix,iy} := \max\left(\xi_{ix,iy}, -r_l \frac{n_{ix,iy}}{k_{ix,iy}}\right)$$

A safety factor $r_l = 1$ for $r = 0.5$ and $r_l = 0.5$ for $r = 1$ is introduced.

In addition to that, the particle source S_n can be limited prior to inserting it into Equation (5.4). The source limiting procedure is based on calculating the characteristic time-scale in the cell:

$$\tau_n^{-1} = \frac{\left|S_n^{ix,iy}\right|}{n_{ix,iy} \cdot vol_{ix,iy}}, \quad \text{if } \tau_n < c_{\Delta t}\Delta t \quad \text{then } S_n^{ix,iy} := \frac{\tau_n}{c_{\Delta t}\Delta t} S_n^{ix,iy}$$

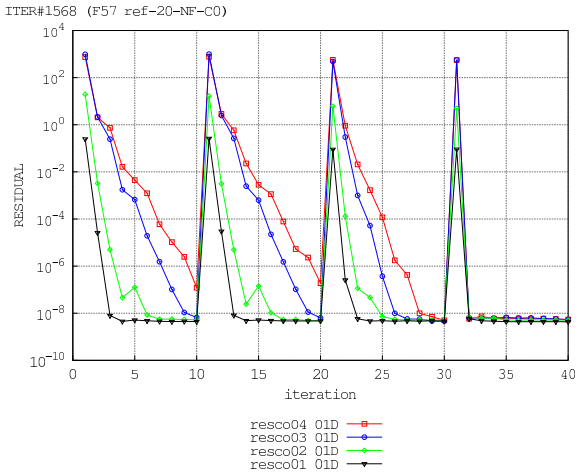

(a) D^+

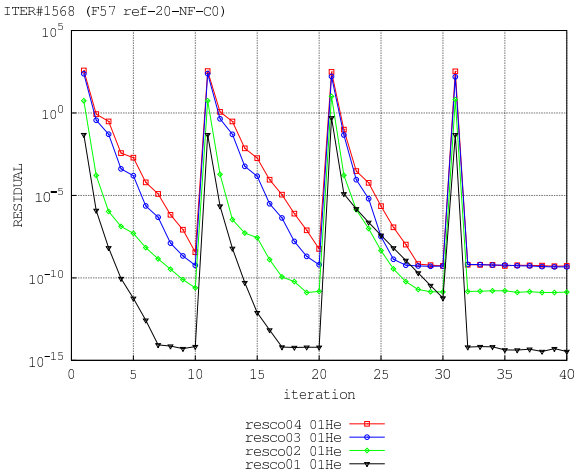

(b) He^+

Figure 5.4: Residuals of the continuity equation for (a) D^+ and (b) He^+. Test of the particle balance correction schemes. The numbers stand for the grid regions: 01 is the core, 02 is the scrape-off-layer, 03 is the inner divertor leg and 04 is the outer divertor leg

The whole source profile is the re-scaled to keep the same total source strength (integral over the grid) the same as before correction. A limiting factor $c_{\Delta t} = 0.01$ is typically used. It has been found that this procedure can significantly distort the final solution in the cases with strong volumetric recombination when a large time-step Δt is applied. In the test runs discussed in the present report $c_{\Delta t}$ was always set to 0: that is, no artificial source limitation is applied at all.

The source limitation has been replaced by an automatic reduction of the time-step in the cells where the sources are too strong. The same time-step $\Delta t^{\beta}_{ix,iy}$ is always applied for all ion fluids which belong to the species β. The correction follows from the cell particle balance:

$$\frac{\check{n}^{\beta}_{ix,iy} - n^{\beta}_{ix,iy}}{\Delta t^{\beta}_{ix,iy}} + \Gamma^{\beta}_{ix,iy} = S^{\beta}_{ix,iy}$$

Here:

$$\Gamma^{\beta}_{ix,iy} = \sum_{\alpha'} \left(fnix^{\alpha'}_{ix,iy} - fnix^{\alpha'}_{ix-1,iy} + fniy^{\alpha'}_{ix,iy} - fniy^{\alpha'}_{ix,iy-1} \right)$$

$$n^{\beta}_{ix,iy} = \sum_{\alpha'} n^{\alpha'}_{ix,iy}, \quad S^{\beta}_{ix,iy} = \sum_{\alpha'} S^{\alpha'}_{n} \, (ix, iy)$$

The sums are calculated over all ion fluids of species β, $\check{n}^{\beta}_{ix,iy}$ is the expected value at the end of the time-iteration, boundary (guard) cells are excluded from this correction. Condition $\check{n}^{\beta}_{ix,iy} > 0$ yields:

$$\check{n}^{\beta}_{ix,iy} = n^{\beta}_{ix,iy} + \left(S^{\beta}_{ix,iy} - \Gamma^{\beta}_{ix,iy} \right) \Delta t^{\beta}_{ix,iy} > 0$$

This inequality is fulfilled automatically if $S^{\beta}_{ix,iy} > \Gamma^{\beta}_{ix,iy}$ (since $n^{\beta}_{ix,iy} > 0$). Otherwise:

$$n^{\beta}_{ix,iy} + \left(S^{\beta}_{ix,iy} - \Gamma^{\beta}_{ix,iy} \right) \Delta t^{\beta}_{ix,iy} > 0 \Rightarrow \Delta t^{\beta}_{ix,iy} < \frac{n^{\beta}_{ix,iy}}{\Gamma^{\beta}_{ix,iy} - S^{\beta}_{ix,iy}} = \Delta t_{max} \tag{5.15}$$

If $S^{\beta}_{ix,iy} < \Gamma^{\beta}_{ix,iy}$ then the local time-step is modified as follows:

$$\text{if } \Delta t > \Delta t_{max} \quad \text{then } \Delta t_{ix,iy} = 0.5 \Delta t_{max} \tag{5.16}$$

The correction is applied on internal iterations each time *after* solving Equation (5.4) for each species.

Experience has shown that even in the run with strong volumetric recombination discussed in Section 6.4 below Equations (5.15), (5.16) never led to correction of local time-step for D^+ ions. Therefore, in the test runs in question this option was normally switched off.

5.5 Can a simplified (0D) correction be applied?

Instead of solving the spatially resolved continuity equations, as described in Section 5.2, one could multiply the whole density profile with a single scaling factor and obtain formally zero error in the global particle balance on the CFD side. The scaling factor ζ_n for each plasma species can be found from the solution of the following equation (written for time-iteration k and internal iteration j):

$$\Gamma_{const} + \Gamma_{out}\zeta_n = S^n_{tot} + N^0_{\Delta t} - N_{\Delta t}\zeta_n \tag{5.17}$$

Where:

$$\Gamma_{out} = \sum_{\alpha'}\sum_{i}\left(S_n^{\alpha'}(j,k) + \frac{n_{\alpha'}(j,k)}{\Delta t} - \frac{n_{\alpha'}(0,k)}{\Delta t} - R_n^{\alpha'}(j,k)\right) - \Gamma_{const}$$

$$S^n_{tot} = \sum_{\alpha'}\sum_{i} S_n^{\alpha'}(j,k), \quad N^0_{\Delta t} = \sum_{\alpha'}\sum_{i}\frac{n_{\alpha'}(0,k)}{\Delta t}, \qquad N_{\Delta t} = \sum_{\alpha'}\sum_{i}\frac{n_{\alpha'}(j,k)}{\Delta t}$$

The sum is calculated over all cells i and ion fluids α', the time-step Δt can be spatially non-uniform. The correction is based on the assumption that the outflux from the computational grid is directly proportional to the density. On boundaries where e.g. constant flux boundary conditions are specified this condition is not fulfilled. Outflux at such boundaries is taken into account separately in Γ_{const}.

The correction has been implemented in B2 at the end of internal iterations. Scaling factor ζ_n is calculated from Equation (5.17), then the density $n_{\alpha'}$ in each cell is multiplied by ζ_n - a special treatment is required at the boundaries for some types of boundary conditions, the sources $S_n^{\alpha'}$ are re-calculated, Equation (1.8), and the iteration is repeated. Approximately 10 such iterations are typically required.

The correction has been tested for the case #1568vk4, same as in Section 4.2. The test has indicated that this procedure leads to long-period self-sustained oscillations and no steady-state solution can be obtained. An example is shown in Figure 5.5 which represents time-traces from the run made with time-step Δt =1e-4 sec and 1e-3 sec in the core. A run with Δt =1e-4 sec in the whole computational has been made as well, but was not continued after one period of similar oscillations was detected. It can be concluded that the correction based on Equation (5.17) is not applicable in practice.

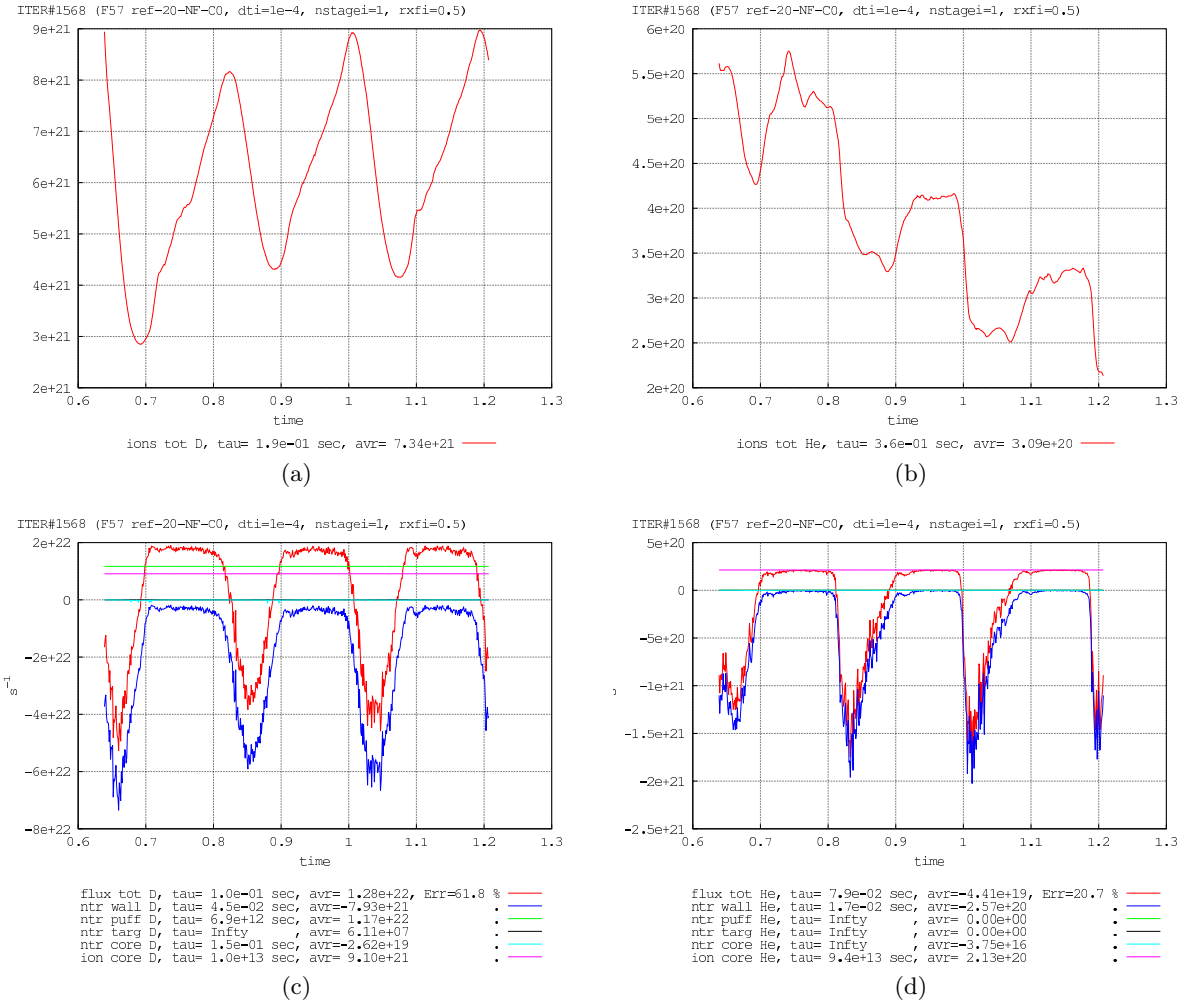

Figure 5.5: Time-tracings of the test with simplified correction of particle balance, see Section 5.5. (a) is the total amount of D ions; (b) is the total amount of He ions; (c) is the D particle balance; (d) is the He particle balance

Chapter 6

Case studies

6.1 Tests with extra continuity iterations

The test case #1568vk4 from Section 4.2 was repeated with one full iteration and 99 extra iterations for particle balance - continuity iterations - described in Section 5.2. Several runs with different number of Monte-Carlo (MC) test particles have been made. They are compared with a series of runs made with small time-step Δt and (full) internal iterations. All test cases are listed in Table 6.1. In this table m is the number of full internal iterations, f_{MC} is the multiplier for the number of MC particles.

In all runs the characteristic time scale τ >10 sec is reached for E_e, E_i, N_D, N_{He} (see Section 1.3 for definition). For separatrix parameters $< n_e >^{sep}$, $< T_e >^{sep}$, $< T_e >^{sep}$, $< Z_{eff} >^{sep}$ the time-scale τ >10 sec with Δt =1e-4 and τ >1.5 sec with Δt =3e-7.

As expected, continuity iterations lead to strong reduction of E_R - the error in the global particle balance due to the CFD residual (see Section 5.1), compared to the error obtained with $m = 1$ and shown in Figures 5.1, 5.2. $< E_R^D >$ becomes smaller than 4e19 s^{-1}, and $< E_R^{He} >$ - smaller than 2e17 s^{-1}. As a result, even without increased number of test particles $\Delta\Gamma_D$ drops almost to the level which without continuity iterations could be achieved only with time-averaging of sources or increased number of particles, compare Table 6.2 and Table 4.5. For He $< E_R^{He} >$ can even be made smaller than in those latter cases.

With continuity iterations the generalized residual *GENRES* obtained in the runs with $m = 1$ are larger than those obtained with $m > 1$ and same number of MC particles, Figures 6.1, 6.2. As one can see from Figure 6.1, *GENRES* can be brought to the same level as with internal iterations by increasing the number of Monte-Carlo particles. The number of particles had to be increased by a factor 40, whereas the time-step is larger by a factor 330. That is, if the same convergence rate is assumed, the run '1e-4x40' is still almost a factor of 10 faster than '3e-7x1', even if the same number of processors is used for the Monte-Carlo part. Continuity iterations reduce residuals of the particle balance but can lead to increase of *GENRES* for other equations. However, comparing Figures 6.1, 6.2 with Figures 4.5, 4.6 (case '1e-4x40' versus '5e-5/1/40') indicates that R is increased by only a factor of ≈2.

Table 6.1: Parameters of tests (#1568vk4) with extra iterations for continuity equations

Notation	Δt, sec	m	f_{MC}
1e-4x1	1e-4	1	1
1e-4x10	1e-4	1	10
1e-4x40	1e-4	1	40
3e-7x1	3e-7	20	1
3e-7x10	3e-7	20	10
3e-7x40	3e-7	20	40

Table 6.2: Particle and energy balance (#1568vk4)

	1e-4x1	1e-4x10	1e-4x40	3e-7x1	3e-7x10	3e-7x40
$\Delta\Gamma_D, \%$	23.19	5.68	0.85	1.39	0.66	0.29
$\Delta\Gamma_{He}, \%$	24.50	2.54	2.31	6.77	3.29	1.98
$\Delta P, \%$	0.39	0.83	0.81	0.74	1.00	1.06

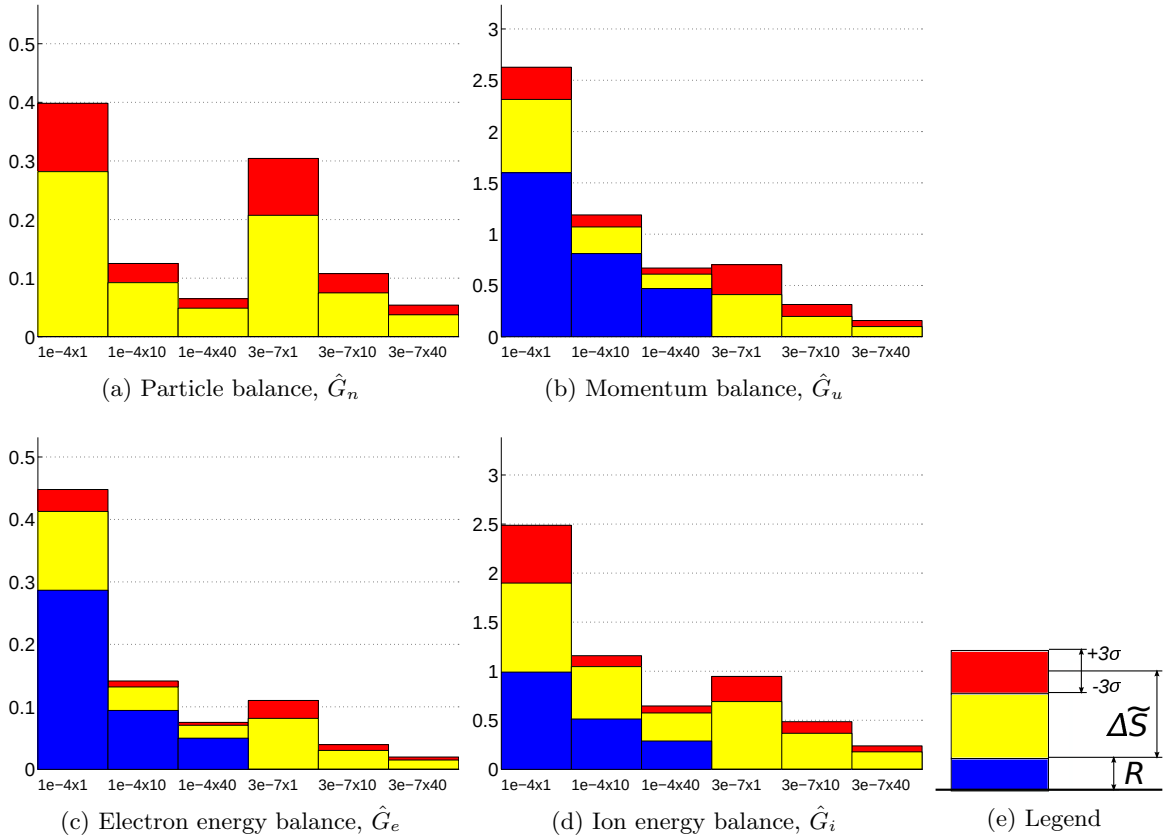

(a) Particle balance, $\hat{G}_n$

(b) Momentum balance, $\hat{G}_u$

(c) Electron energy balance, $\hat{G}_e$

(d) Ion energy balance, $\hat{G}_i$

(e) Legend

Figure 6.1: Normalized generalized residuals, Equation (2.11), for test cases listed in Table 6.1. Particle $\hat{G}_n$ and momentum $\hat{G}_u$ residuals are given for D

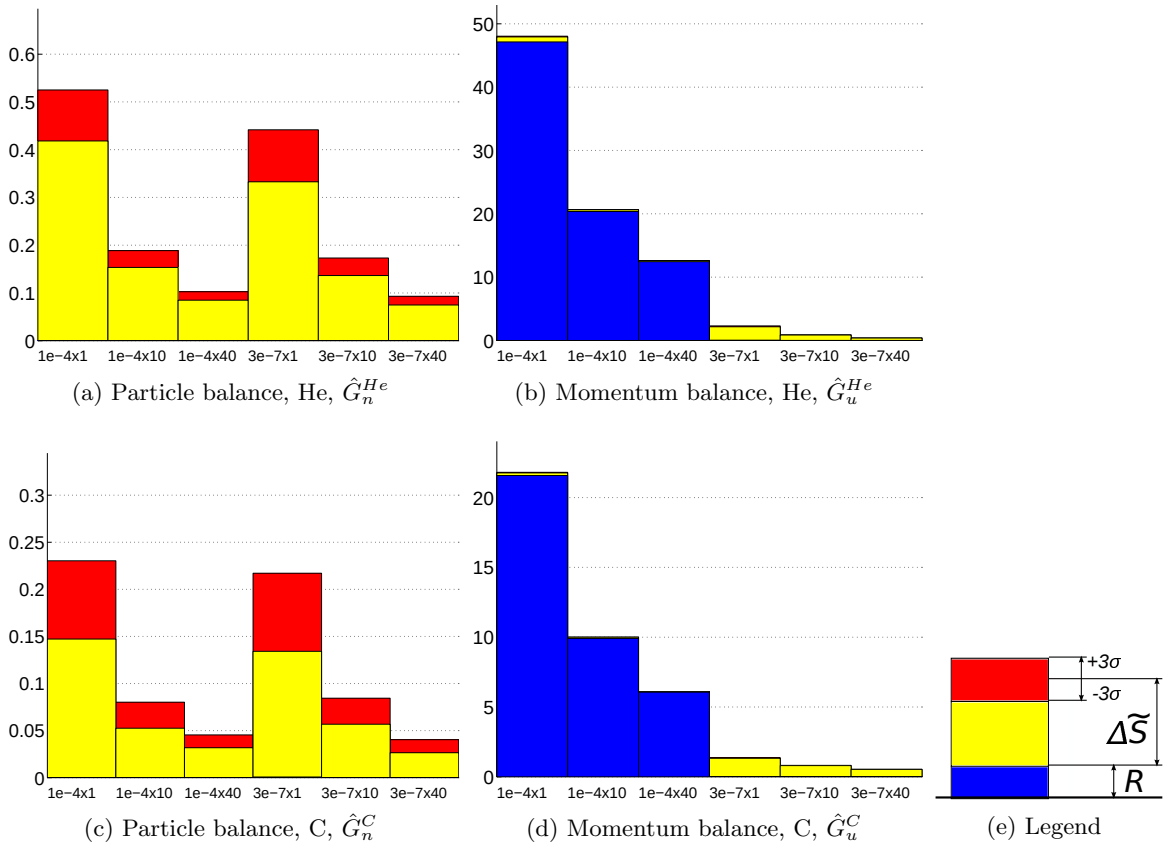

(a) Particle balance, He, $\hat{G}_n^{He}$ (b) Momentum balance, He, $\hat{G}_u^{He}$

(c) Particle balance, C, $\hat{G}_n^{C}$ (d) Momentum balance, C, $\hat{G}_u^{C}$ (e) Legend

Figure 6.2: Normalized generalized residuals, Equation (2.11), for test cases listed in Table 6.1, particle and momentum balance for impurities

The *GENRES* for impurity momentum balance with $m = 1$ is always very large, Figure 6.2, and always much larger than that with $m > 1$ even with increased number of MC particles. On the other hand, with $m > 1$ while R is decreased the time-derivative is increased and becomes the dominant part of the error. Presumably, the time-derivative term reflects oscillations remaining in the solution. Moreover, high spikes are seen on the time-traces of *GENRES* for momentum balance of impurities, whereas with $m = 1$ the time-trace appears steady. An example is shown in Figure 6.3. Here, same as in Sections 4.1, 4.2 the *GENRES* at the last time-iteration are shown on the diagrams of Figures 6.1, 6.2. This way of comparison might be not appropriate in the presence of spikes, but the time-averaged values of $\hat{G}_u^{He}$ and $\hat{G}_u^{C}$ are apparently smaller with $m > 1$ than with $m = 1$ as well.

Principal engineering parameters of divertor operation calculated in the model runs listed in Table 6.1 are compared in Table 6.3. Those are parameters which characterize impurity removal from plasma - Z_{eff} and concentration of He averaged over magnetic separatrix: $< Z_{eff}^{sep} >$ and C_{He}^{erp}, and peak heat flux densities on the inner and outer divertor targets q_{pk}^{in} and q_{pk}^{out}. The difference in those parameters between cases '1e-4x1' and '3e-7x1' is relatively large, but an increase of the number of MC particles brings the numbers very close to each other. The solution obtained with $m > 1$ does not exibit significant variation as the number of test particles increases.

Calculated profiles of the plasma parameters are compared in Figure 6.4. One can see a relatively large variation between '1e-4x1' and '1e-4x10'. The difference between '1e-4x10' and '1e-4x40' is smaller, but is still relatively large for the target temperatures. With $m > 1$ the effect of increasing the number of MC particles is somewhat smaller. Discrepancies between the solutions obtained with $m > 1$ and $m = 1$ are reduced with increased number of MC particles.

Without internal iterations the boundary conditions are not fulfilled with high precision. An

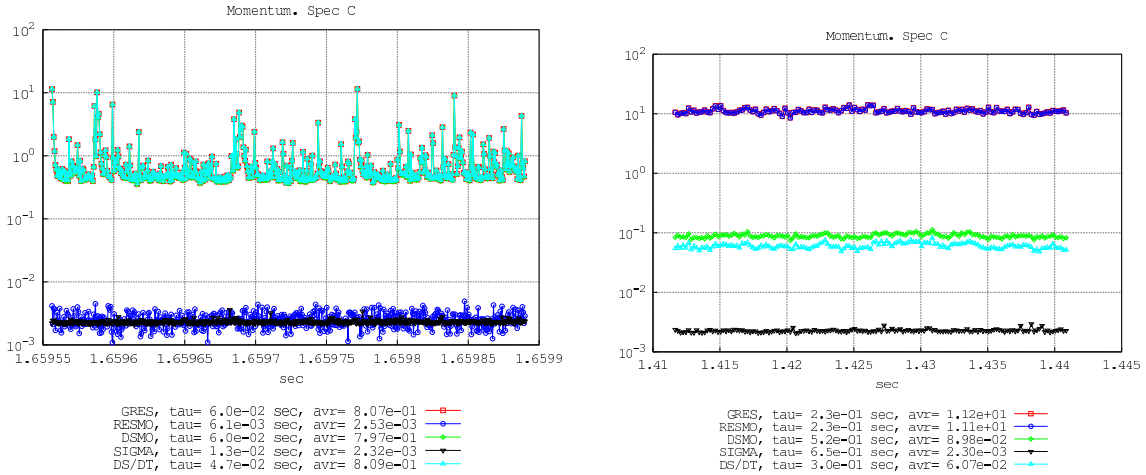

(a) (b)

Figure 6.3: Time-traces of *GENRES* for momentum balance of C: a) with 20 internal iterations and Δt=3e-7 sec; b) with 1 full iteration, 99 extra continuity iterations and Δt=1e-4 sec.

Table 6.3: Calculated principal engineering parameters (#1568vk4)

	1e-4x1	3e-7x1	1e-4x10	3e-7x10	1e-4x40	3e-7x40
$< Z_{eff}^{sep} >$	1.53	1.50	1.50	1.50	1.49	1.50
C_{He}^{sep}, %	7.20	6.45	6.47	6.45	6.43	6.46
q_{pk}^{in}, MW/m^2	8.43	6.01	5.66	5.87	5.94	5.94
q_{pk}^{out}, MW/m^2	10.22	8.08	8.27	8.10	8.17	8.08

example is shown in Figure 6.5 for the electron sheath transmission factor $\gamma_e = \frac{Q_e}{\Gamma_e T_e}$. Here Q_e is the density of the heat flux incident to the divertor target and transmitted by electrons, Γ_e is the incident electron particle flux density, and T_e is the electron temperature. The nominal value of γ_e is fixed at 5.1. The parallel Mach number at the divertor targets prescribed at 1 in the run '1e-4x40' varies between 0.985 and 1.015.

In addition to tests described above, it was also tried to extend the continuity iterations and to correct both particle and momentum balance. That is, a first internal iteration is performed as described in Section 1.2, with exception of item 9. On the subsequent iterations only momentum and particle balances are updated: energy balance - items 6,7,8 - is skipped. A test made for case #1568vk4 has shown that with the small number of incomplete iterations (≈10) this procedure is not efficient in reducing *GENRES*, and with large number of iterations (≈100) it is too unreliable: at some time-iteration the incomplete iterations may even start to diverge and the solution does not converge to any steady-state at all.

6.2 Can continuity iterations be combined with averaging?

An attempt to combine the continuity iterations with time-averaging of sources, Section 3, led to strong regular oscillations remaining in the solution. An example for the single-ion test case #2013vk4, see Section 4.1, is shown in Figure 6.6. This is a simulation with Δt=1e-4 sec, one full iteration and 499 extra particle balance iterations, averaging phase with $L = 50$. Such large number of continuity iterations ensures convergence of the CFD particle balance residuals R down to machine precision on each time-iteration.

The reason for the sawtooth-like oscillations seen in Figure 6.6 is not clear. It initially was suspected that they could be caused by volume recombination, but complete elimination of the volume recombination strata did not remove the oscillations. Switching off re-scaling, Equation (3.2), for all source terms except particle sources S_n also does not mitigate them

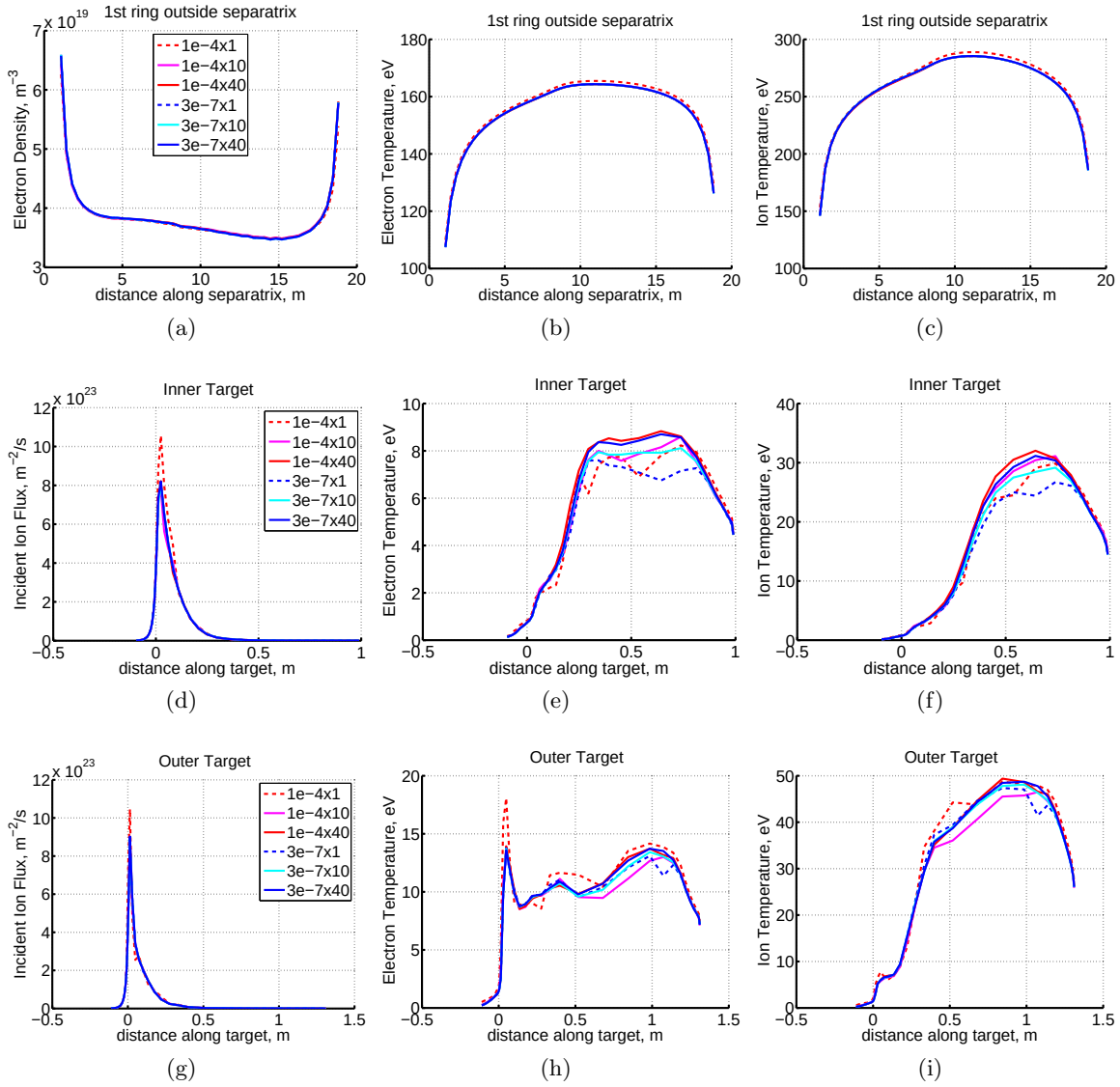

Figure 6.4: Solutions obtained in the test calculations listed in Table 6.1. Positions of Inner and Outer Targets are shown in Figure 1.1. "Distance along target" is zero at the intersection with magnetic separatrix, positive values point upwards. "Separatrix" is the dashed line in Figure 1.1, "distance along separatrix" goes from inboard to outboard side.

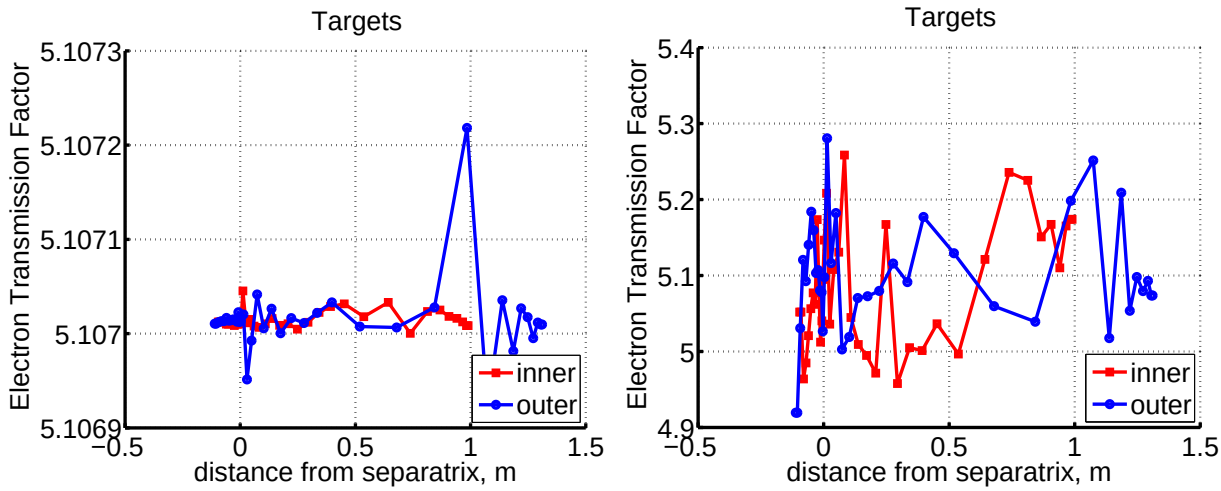

(a) #1568vk4, 3e-7x40 (b) #1568vk4, 1e-4x40

Figure 6.5: Electron sheath transmission factor $\gamma_e = \frac{Q_e}{\Gamma_e T_e}$ in the simulations a) with and b) without internal iterations. $\gamma_e = 5.1$ is the nominal value. "Inner" and "outer" stands for inner and outer divertor targets respectively.

either. The oscillations could be suppressed by reducing the time-step: in the case in question (#2013vk4) they could still be observed with Δt=5e-5 sec, but almost disappeared with Δt=2e-5 sec. "Almost disappeared" means here that regular sawtooth-like patterns became indistinguishable from the "normal" statistical noise in the solution.

Time-traces of the multi-ion test case #1568vk4 obtained with time-averaging combined with continuity iterations also could be interpreted as having regular oscillation patterns, although much less pronounced than in #2013vk4 case. Since there is no clear answer about the nature of the anomalous behavior described above and its potential damage to the solution, it must be recommended to refrain from applying continuity iterations in combination with averaging. It is found to be more efficient for reducing *GENRES* to increase the number of MC particles and to use large Δt instead of applying averaging and be forced to decrease Δt.

6.3 Can the time-step be increased?

All tests with extra continuity iterations discussed in Section 6.1 were performed with Δt=1e-4 sec. What happens if the time-step is increased even further? It turns out that with too large time-step the residuals in the core zone inside the magnetic separatrix (see Figure 1.1) become too large. An example for the calculation made with f_{MC}=10 is shown in Figure 6.7. The core *GENRES* are dominated by the CFD residual R, with exception of particle balance for which $\Delta\tilde{S}$ (`deltas` on the plot) is the dominant term. *GENRES* for momentum and particle balance of C and He have the same behavior. Large residuals result in onset of strong non-physical oscillations of the SOL and divertor parameters. It is to bee noted that *GENRES* in SOL and divertor legs do not experience such dramatic growth as in the core.

It has been also found that without continuity iterations the restriction on the time-step can be relaxed. Case #1568vk4 with $m = 1$ and f_{MC}=40 could be run with Δt=1e-3 sec without increase of residuals. With Δt=1e-2 sec a similar effect as in Figure 6.7 was observed [1].

It can be also added at this point that all calculations described in the present report were performed with relaxation parameter $r = 0.5$. A test run made with $r = 1$ (#1568vk4, $m = 1$,

[1] Apparently, artificial spin-up of flow on the closed flux surfaces in B2 code was already detected in the past. Parallel flow suppression through magnetic pumping term was introduced to solve this problem. This option has not been re-activated

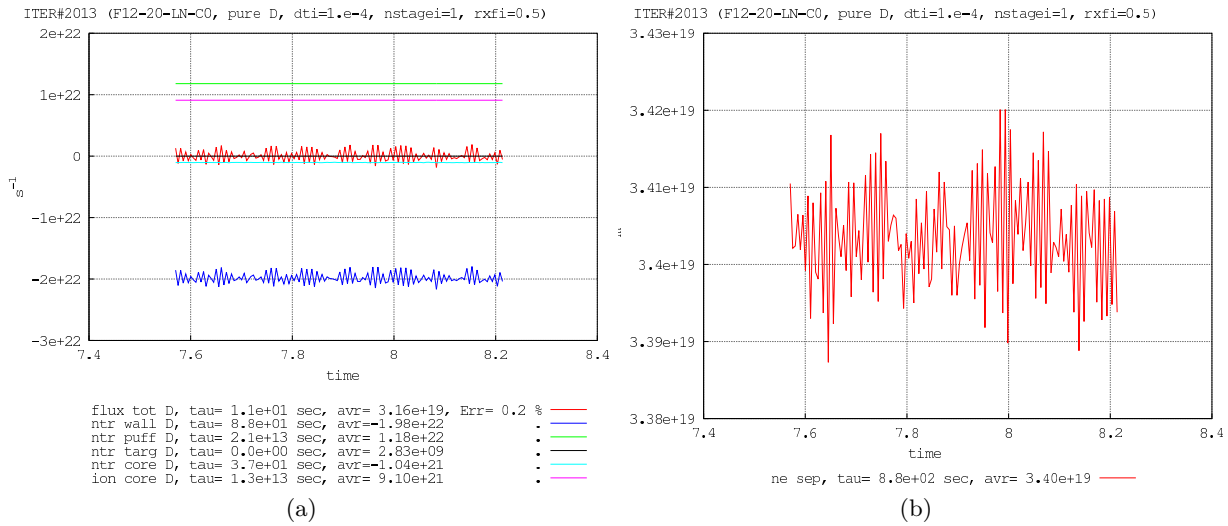

(a) (b)

Figure 6.6: Sawtooth-like oscillations which appear when continuity iterations, Section 5.2, are used in combination with the time-averaging of sources, Section 3. Test case #2013vk4, see Section 4.1.

f_{MC}=1) did not reveal any significant differences compared to $r = 0.5$ in terms of *GENRES* and balances.

6.4 A use case study

As it could be seen in Section 6.1, the solution obtained with continuity iterations and relatively small number of the MC test particles is already close to the refined solution obtained with increased number of particles. This observation suggest the following practical way of making simulations: a "fast" run on the relatively small number of processors is brought to a steady-state, and then continued with increased number of test particles to refine the solution. This approach has been tried for the ITER case #1542vk4 which has exactly same model as #1568vk4, but higher gas puffing rate Γ_{puff}=1.55e23 s^{-1} and higher input power P_{SOL}=100 MW. High puffing rate leads to divertor density which is substantially larger than in #1568vk4: p_{PFR}=11 Pa, and higher radiation fraction - 70 % of P_{SOL} is radiated. The final solution has a cold divertor plasma - especially on the inner side - with strong volumetric recombination and plasma momentum losses due to ion-neutral friction.

All stages of the simulation are listed in Table 6.4. Variables t_s and t_e in this table are the start and end time of each stage in terms of physical time of the model. This sequence of runs has to mimic an approach to an approximate solution and its refinement as it can be done in practical ITER computations. The run was started from #1568vk4 as initial solution with Δt=1e-4, $m = 1$ and 99 extra iterations for continuity equations (for all species). Regular number of MC particles, f_{MC}=1, at the beginning. After reaching a steady state the simulation was continued with increased number of MC particles, f_{MC}=10, and then continued further with f_{MC}=40. Then, continuity iterations for D and C were switched off - they were left only for He, and the run was continued with f_{MC}=40. In Table 6.4 this last stage is named '1e-4x40*'. The table also lists two separate runs made with $m = 20$ and small time-step Δt=2e-7 for comparison.

Behavior of the He particle content, Figure 6.8b, has to be further explained. It became clear from the beginning that convergence of the He content in a natural way will require very long physical time to be modelled and, thus, will make the overall run-time of the model prohibitively long. For speed-up the time-step for the He particle balance (only for those two equations) was

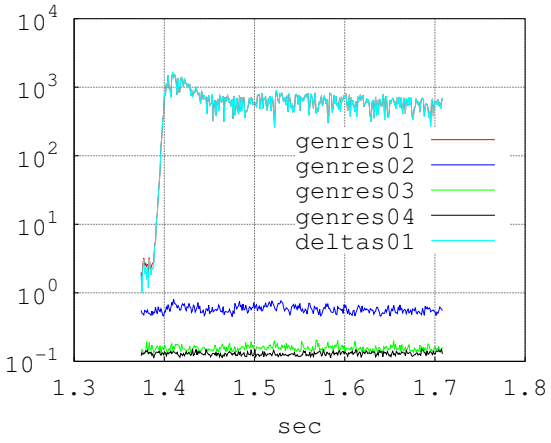

(a) Particle balance, D

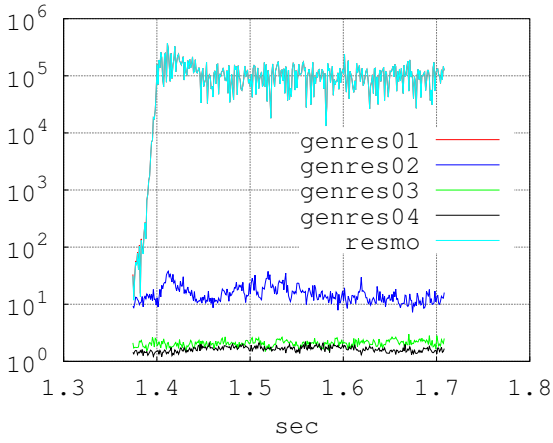

(b) Momentum balance, D

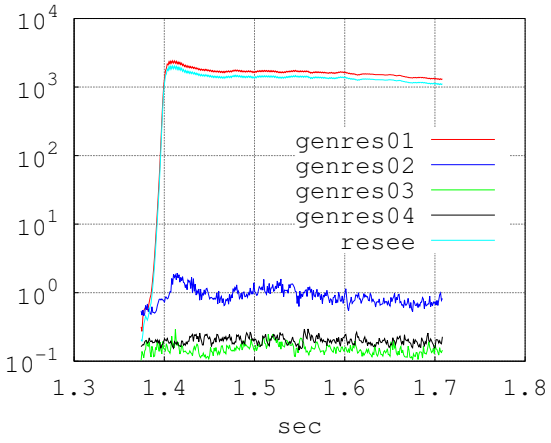

(c) Electron energy balance

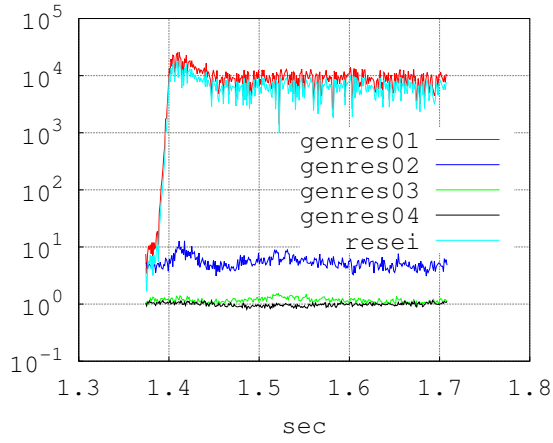

(d) Ion energy balance

Figure 6.7: Time-traces of generalized residuals calculated for #1568vk4 with continuity iterations and Δt=1e-3 sec. The numbers stand for the grid regions: 01 is the core zone inside magnetic separatrix (see Figure 1.1), 02 is the scrape-off-layer, 03 is the inner divertor leg and 04 is the outer divertor leg

Table 6.4: Parameters of tests with high density divertor (#1542vk4)

Notation	t_s, sec	t_e, sec	Δt, sec	m	f_{MC}
1e-4x1	1.76	2.58	1e-4	1	1
1e-4x10	2.58	2.76	1e-4	1	10
1e-4x40	2.76	2.78	1e-4	1	40
1e-4x40*	2.78	2.89	1e-4	1	40
2e-7x1	-	-	2e-7	20	1
2e-7x10	-	-	2e-7	20	10

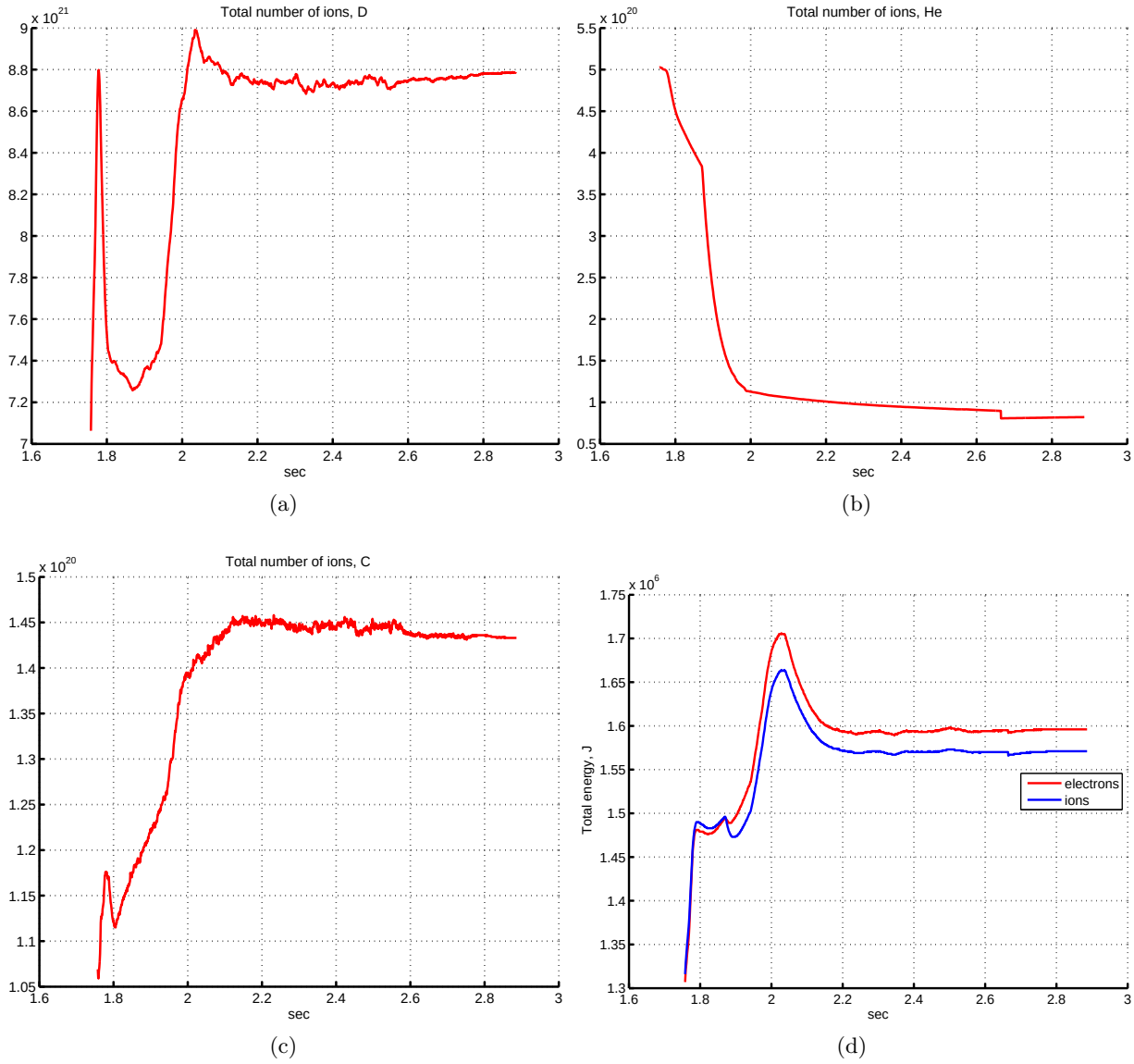

Figure 6.8: Time-tracings of the total number of ions and total diamagnetic energy. Case #1542vk4 , Table 6.4

increased to 1e-3 sec. This increase of Δt_{He} manifests itself as rapid drop of the number of He ions between t =1.87 sec t =1.99 sec. Further, traces of some negative effects on the momentum balance have been noticed, therefore, as a precaution measure at t =1.99 sec Δt_{He} was returned back to 1e-4 sec and the He particle balance was converged further in the natural way. It cannot be said with certainty that the applied way of speeding up the He convergence was indeed harmful - the issue was not further investigated. At t =2.67 sec another speed-up trick was used: multiplication of the initial He density by a factor 0.9 when the run is re-started for continuation. The effect of this multiplication is seen as step in Figure 6.8b.

Time-tracings of the run which include all stages are presented in Figures 6.8-6.10. Characteristic times (see Section 1.3) at the end of each stage are >9 sec (>4 sec for N_{He}, N_C). As expected, the residuals (*GENRES*) are reduced with increased number of particles, Figures 6.10, 6.11. However, for momentum balance this reduction is apparently less than by a factor $\sqrt{f_{MC}}$. From Figures 6.12, 6.13 where diagrams of *GENRES* at the end of each stage are shown it becomes apparent that R for momentum balance practically does not reduce with increased f_{MC}, and the values are large, especially for impurities.

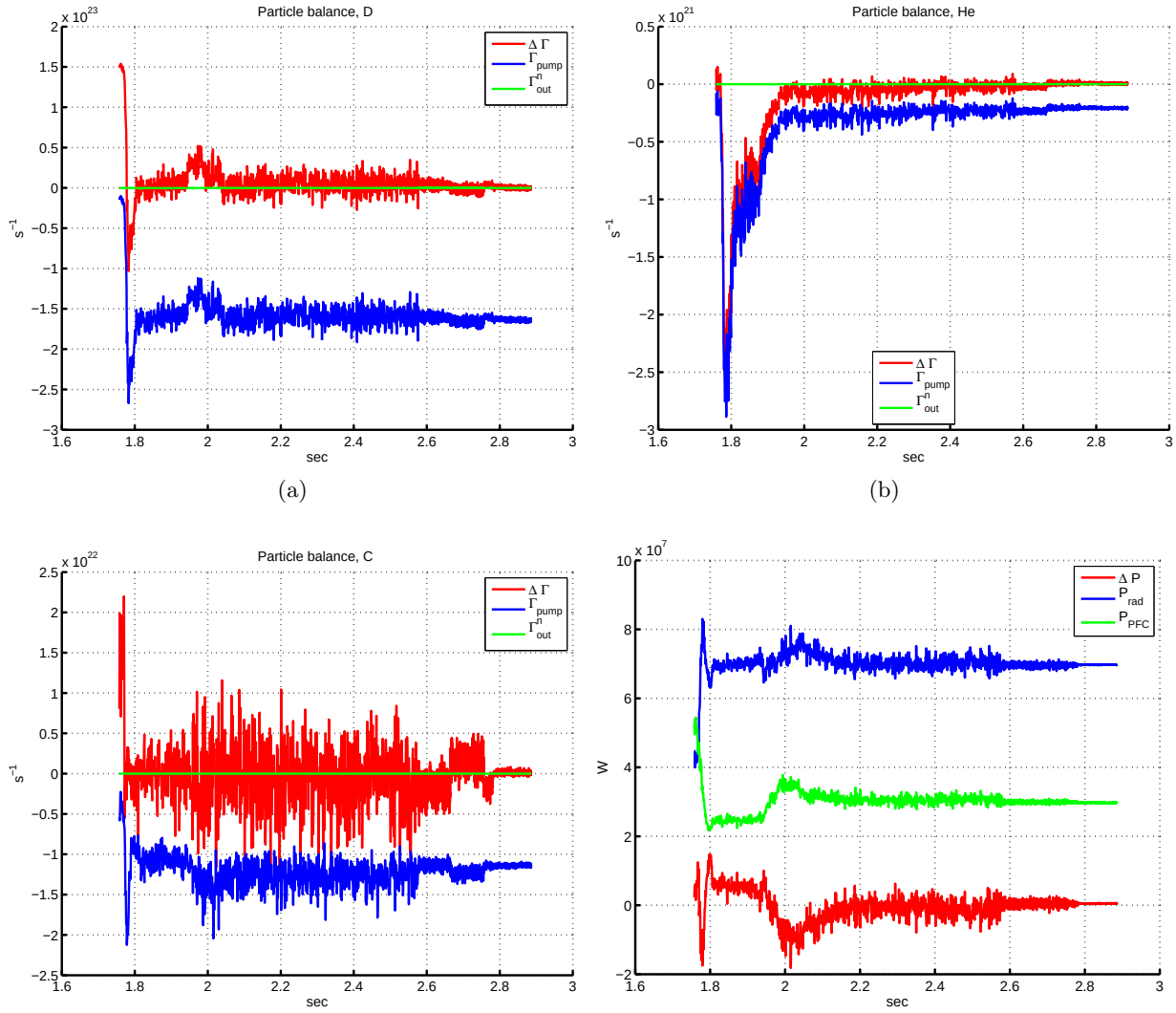

Figure 6.9: Time-tracings of the particle and energy balance, see Equations (1.9) and (1.10), Section 1.3. Case #1542vk4, Table 6.4

Table 6.5: Particle and energy balance (#1542vk4)

	1e-4x1	1e-4x10	1e-4x40	1e-4x40*	2e-7x1	2e-7x10
$\Delta\Gamma_D, \%$	1.40	0.70	1.82	0.20	0.59	1.46
$\Delta\Gamma_{He}, \%$	4.72	3.45	3.26	3.14	7.07	4.96
$\Delta P, \%$	0.39	0.43	0.33	0.49	0.33	0.34

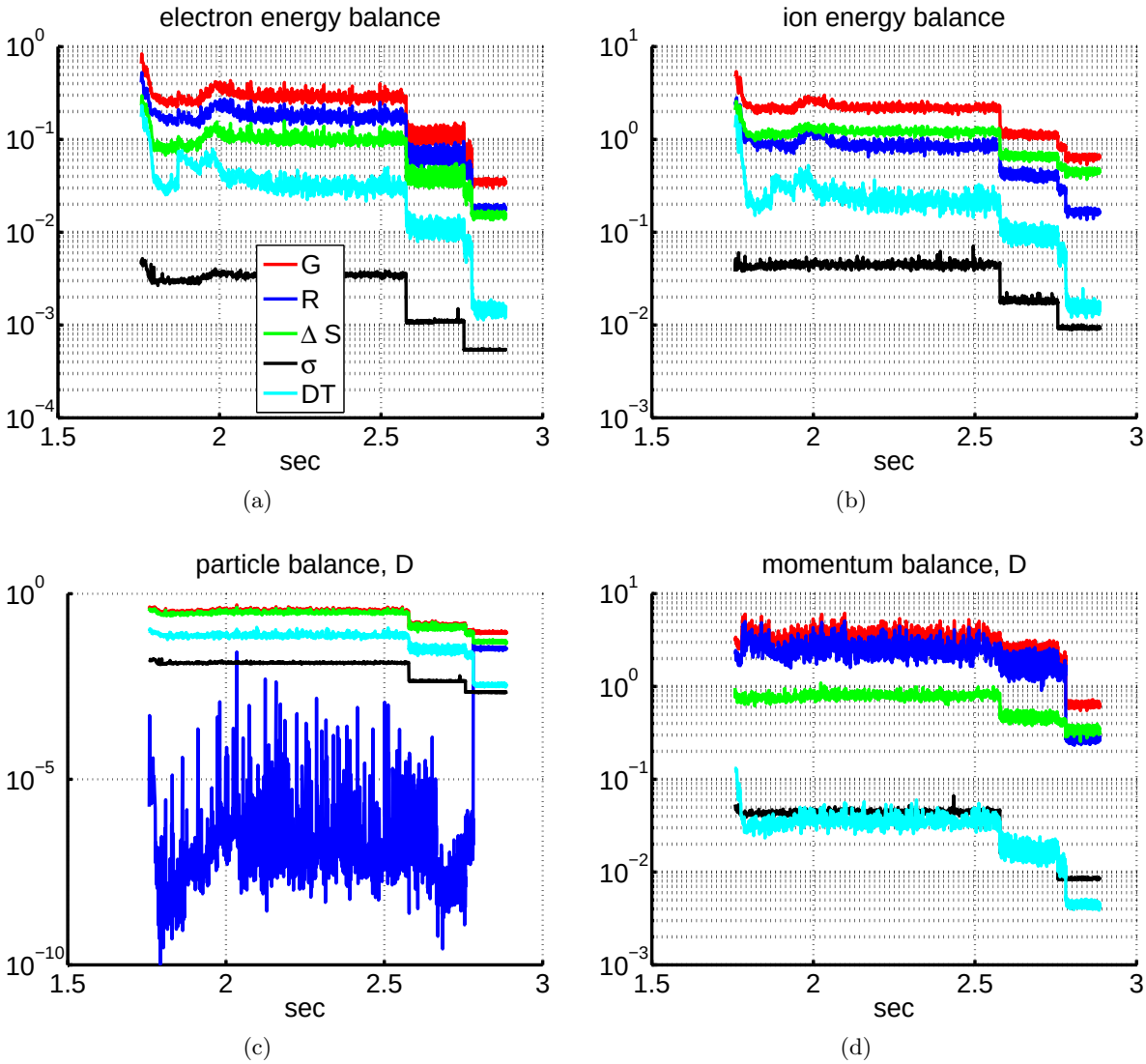

Figure 6.10: Time-tracings of *GENRES* for energy and main ions, case #1542vk4 , Table 6.4. In the legend G, R, ΔS and σ are normalized generalized residuals G and its terms R, $\Delta\tilde{S}$ and σ, Equation (2.9), DT is the time derivative (included in $\Delta\tilde{S}$)

The decision to continue the simulation with continuity iterations kept only for He was based on two considerations. First, it was suspected that continuity iterations could be the main reason of "damaging" the momentum balance. Second, one could see that with f_{MC}=40 already for the low-density case, Section 4.2, the error in the particle balance for main ions is almost on acceptable level, and the relative error is expected to be smaller with higher gas puffing rate. To stay on the safe side, continuity iterations were left for He. The test results have confirmed those considerations. Without continuity iteration R for momentum balance indeed drops significantly, Figures 6.10d, 6.12b and 6.11b, 6.11d, 6.13b, 6.13d. At the same time, the relative error in particle balance $\Delta\Gamma_D$ stays small, see Table 6.5 and Figure 6.9a - much smaller than in the low density case #1568vk4. Generally speaking, in the low density (low gas puff) case the continuity iterations are required to get acceptable particle balance, and their negative effect on the convergence (residuals) of other equations is moderate. In the high density case with cold divertor the negative effect is much larger, however, the extra correction of particle balance gets less important because even without this correction the error in the global particle balance due to the CFD residual R is smaller than the throughput.

As can bee seen from Figures 6.12, 6.13, without continuity iterations for D and C the

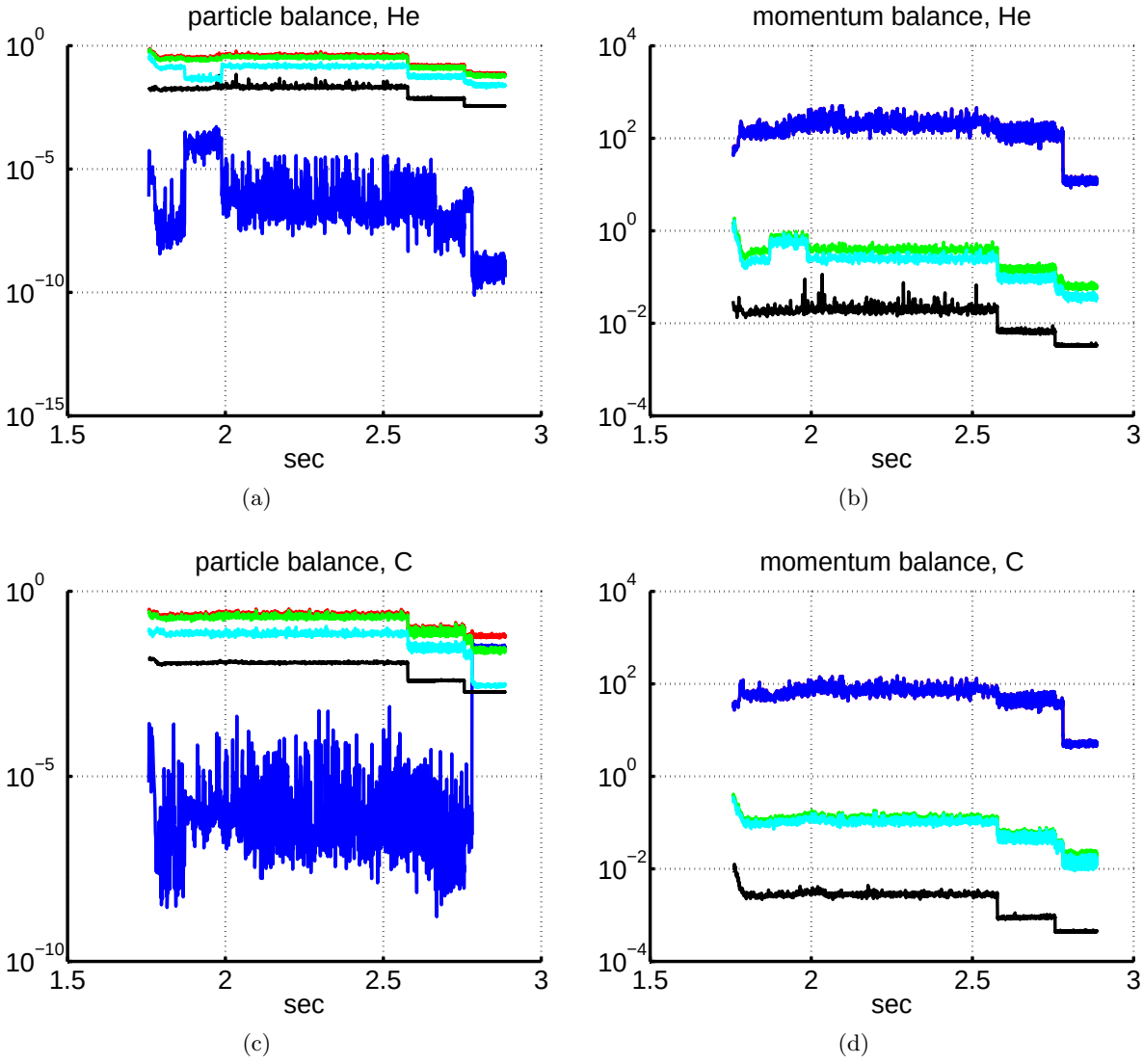

Figure 6.11: Time-tracings of *GENRES* for the particle and momentum balance of impurities, case #1542vk4 , Table 6.4. Same legend as in Figure 6.10

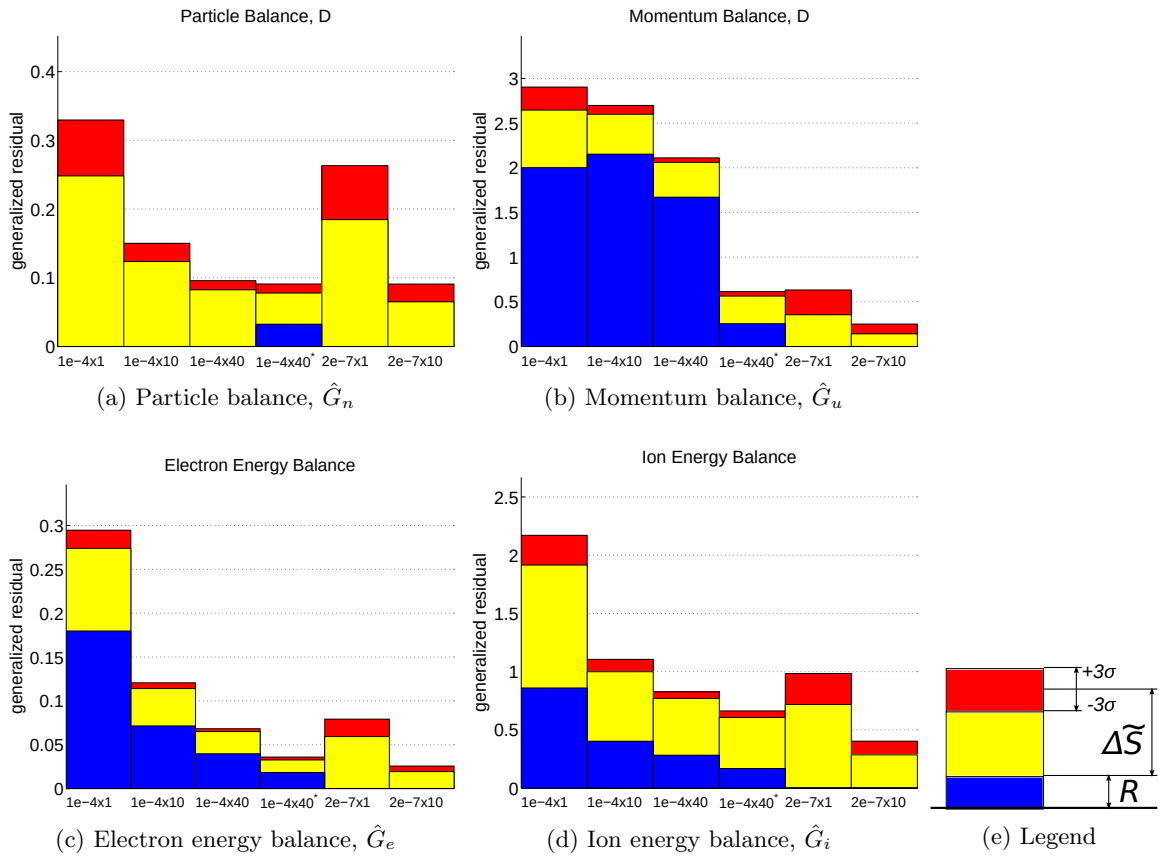

(a) Particle balance, $\hat{G}_n$ (b) Momentum balance, $\hat{G}_u$

(c) Electron energy balance, $\hat{G}_e$ (d) Ion energy balance, $\hat{G}_i$ (e) Legend

Figure 6.12: Normalized generalized residuals, Equation (2.11), for test cases listed in Table 6.4. Particle $\hat{G}_n$ and momentum $\hat{G}_u$ residuals are given for D

GENRES is as small as with with $m = 20$ and f_{MC}=1, and for the electron energy balance even as small as in the case '2e-7x10'. However, *GENRES* for the momentum balance of impurities stays > 1 and is still much larger than in the runs with $m = 20$, Figures 6.13b, 6.13d. For completness, numerical values of the individual terms of *GENRES* are summarised in Table 6.6.

The set of calculated plasma profiles is shown in Figure 6.14. Solutions obtained with the highest number of MC particles with and without internal iterations deviate very insignificantly from each other - case '1e-4x40*' versus '2e-7x10'. Surprisingly, the solution obtained with continuity iterations for all species '1e-4x40' does not deviate significantly from the former two as well, despite much higher *GENRES* for momentum balance. Significant disagreement can bee seen only for the calculations made with f_{MC}=1. One can say that in the practical sense even the "worst case" '1e-4x1' is in rather good agreement with the rest. See also the engineering output parameters in Table 6.7.

Further insight into the accuracy of coupled CFD-MC calculations without internal iterations is given by Figures 6.15 and 6.16 where fulfillment of boundary condition and the integral momentum balance are shown for case '1e-4x40*'. Electron sheath transmission factor γ and parallel Mach number M, Figure 6.15, noticeably deviate from their prescribed values γ=5.1 and M=1. The level of error is similar to the low density case #1568vk4, Figure 6.5. The result obtained for '1e-4x40' - with continuity iterations for D and C - is much worse: spikes in the reconstructed γ reach values of 10. A description of the diagram for the integral parallel momentum balance shown in Figure 6.16 can be found in [15] and is not repeated here. Apparently, even with very large number of MC particles the error can locally remain comparable to the terms of the solution itself.

Total wall-clock time required for the simulations can be estimated from the data in Table 6.8.

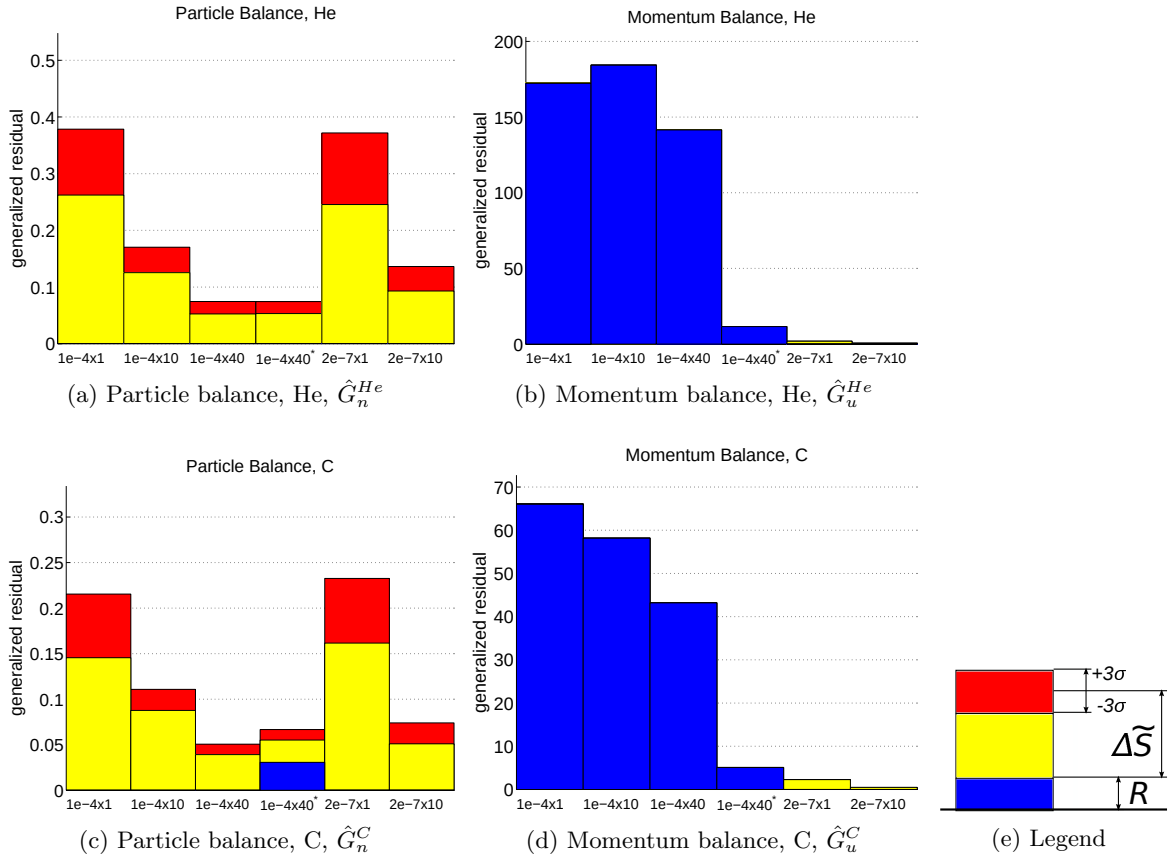

(a) Particle balance, He, $\hat{G}_n^{He}$

(b) Momentum balance, He, $\hat{G}_u^{He}$

(c) Particle balance, C, $\hat{G}_n^{C}$

(d) Momentum balance, C, $\hat{G}_u^{C}$

(e) Legend

Figure 6.13: Normalized generalized residuals, Equation (2.11), for test cases listed in Table 6.4, particle and momentum balance for impurities

Table 6.6: Individual terms of *GENRES* for the test case #1542vk4

case	1e-4x1	1e-4x10	1e-4x40	1e-4x40*	2e-7x1	2e-7x10
$\hat{R}_n$	2.0e-07	2.2e-08	4.4e-07	3.2e-02	4.2e-05	2.0e-05
$\Delta\tilde{S}_n$	2.9e-01	1.4e-01	8.9e-02	5.2e-02	2.2e-01	7.8e-02
$\hat{\Sigma}_n$	9.9e-02	8.1e-02	1.3e+00	4.1e-02	2.1e-01	7.4e-02
$\hat{D}_n$	6.6e-02	3.4e-02	2.3e-02	3.6e-03	2.3e-01	7.7e-02
$\hat{\sigma}_n$	1.4e-02	4.4e-03	2.2e-03	2.2e-03	1.3e-02	4.3e-03
$\hat{R}_u$	2.0e+00	2.2e+00	1.7e+00	2.6e-01	3.5e-04	2.1e-04
$\Delta\tilde{S}_u$	7.7e-01	5.0e-01	4.2e-01	3.3e-01	4.9e-01	2.0e-01
$\hat{\Sigma}_u$	6.2e-01	2.8e-01	1.5e-01	1.5e-01	1.1e+00	4.1e-01
$\hat{D}_u$	3.0e-02	1.7e-02	1.2e-02	4.6e-03	4.8e-01	1.9e-01
$\hat{\sigma}_u$	4.3e-02	1.7e-02	8.4e-03	8.4e-03	4.6e-02	1.8e-02
$\hat{R}_e$	1.8e-01	7.1e-02	4.0e-02	1.8e-02	8.3e-06	4.1e-06
$\Delta\tilde{S}_e$	1.0e-01	4.6e-02	2.7e-02	1.6e-02	6.9e-02	2.3e-02
$\hat{\Sigma}_e$	5.3e-02	1.9e-02	1.3e-02	9.3e-03	2.5e-02	1.8e-02
$\hat{D}_e$	3.6e-02	1.1e-02	7.0e-03	1.6e-03	5.9e-02	1.9e-02
$\hat{\sigma}_e$	3.5e-03	1.1e-03	5.4e-04	5.4e-04	3.3e-03	1.1e-03
$\hat{R}_i$	8.6e-01	4.0e-01	2.8e-01	1.7e-01	5.9e-05	3.0e-05
$\Delta\tilde{S}_i$	1.2e+00	6.5e-01	5.2e-01	4.7e-01	8.5e-01	3.4e-01
$\hat{\Sigma}_i$	4.9e-01	3.4e-01	1.3e-01	1.9e-01	3.0e-01	4.2e-01
$\hat{D}_i$	2.4e-01	9.1e-02	6.0e-02	1.6e-02	4.5e-01	2.2e-01
$\hat{\sigma}_i$	4.3e-02	1.8e-02	9.4e-03	9.4e-03	4.4e-02	2.0e-02
$\hat{R}_n^{He}$	4.1e-07	8.4e-08	7.8e-07	4.1e-10	1.2e-04	6.1e-05
$\Delta\tilde{S}_n^{He}$	3.2e-01	1.5e-01	6.4e-02	6.4e-02	3.1e-01	1.1e-01
$\hat{\sigma}_n^{He}$	1.9e-02	7.5e-03	3.6e-03	3.5e-03	2.1e-02	7.2e-03
$\hat{D}_n^{He}$	1.4e-01	6.2e-02	2.7e-02	2.3e-02	3.3e-01	1.1e-01
$\hat{R}_u^{He}$	1.7e+02	1.8e+02	1.4e+02	1.2e+01	2.7e-02	1.3e-02
$\Delta\tilde{S}_u^{He}$	3.9e-01	1.7e-01	8.1e-02	6.4e-02	1.9e+00	6.4e-01
$\hat{\sigma}_u^{He}$	1.9e-02	6.9e-03	3.3e-03	3.3e-03	1.9e-02	6.9e-03
$\hat{D}_u^{He}$	2.5e-01	1.1e-01	5.2e-02	3.5e-02	1.9e+00	6.3e-01
$\hat{R}_n^{C}$	3.5e-07	3.9e-08	6.0e-07	3.1e-02	1.2e-04	1.2e-04
$\Delta\tilde{S}_n^{C}$	1.8e-01	9.9e-02	4.5e-02	3.0e-02	2.0e-01	6.2e-02
$\hat{\sigma}_u^{C}$	1.2e-02	3.8e-03	1.9e-03	1.9e-03	1.2e-02	3.8e-03
$\hat{D}_n^{C}$	6.0e-02	3.3e-02	1.7e-02	3.0e-03	1.8e-01	5.9e-02
$\hat{R}_u^{C}$	6.6e+01	5.8e+01	4.3e+01	5.1e+00	8.2e-03	3.8e-03
$\Delta\tilde{S}_u^{C}$	1.2e-01	5.9e-02	2.9e-02	2.1e-02	2.3e+00	4.8e-01
$\hat{\sigma}_u^{C}$	2.9e-03	8.9e-04	4.4e-04	4.5e-04	3.1e-03	8.7e-04
$\hat{D}_u^{C}$	9.6e-02	5.3e-02	2.6e-02	1.6e-02	2.3e+00	4.8e-01

Table 6.7: Calculated principal engineering parameters (#1542vk4)

	1e-4x1	1e-4x10	1e-4x40	1e-4x40*	2e-7x1	2e-7x10
$< Z_{eff}^{sep} >$	1.46	1.45	1.45	1.45	1.45	1.45
C_{He}^{sep}, %	0.98	0.84	0.84	0.85	0.84	0.85
q_{pk}^{in}, MW/m^2	3.97	3.95	3.95	3.95	3.82	3.91
q_{pk}^{out}, MW/m^2	4.62	4.41	4.12	4.04	4.02	4.08

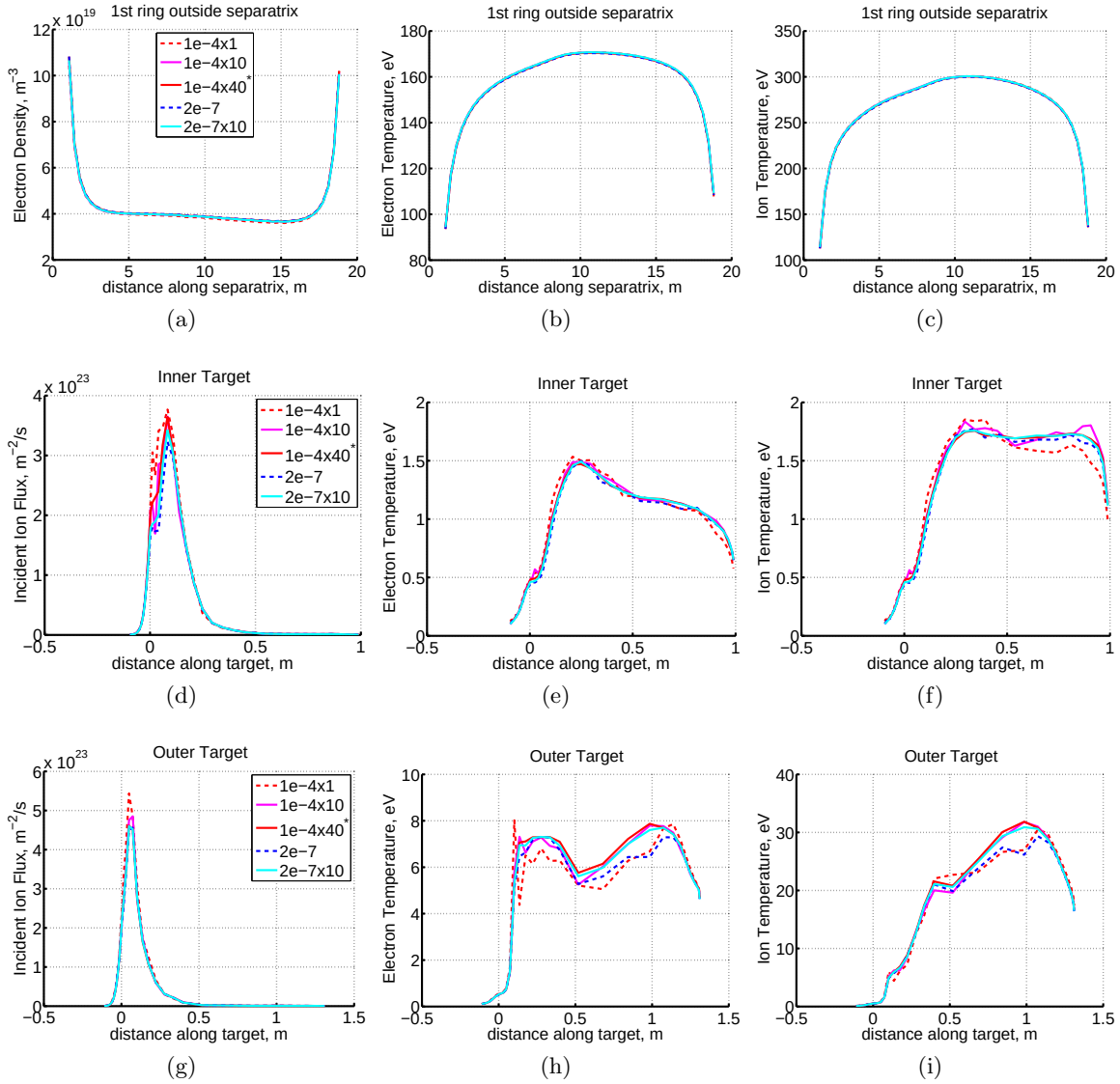

Figure 6.14: Solutions obtained in the test calculations, Table 6.4. Positions of Inner and Outer Targets are shown in Figure 1.1. "Distance along target" is zero at the intersection with magnetic separatrix, positive values point upwards. "Separatrix" is the dashed line in Figure 1.1, "distance along separatrix" goes from inboard to outboard side.

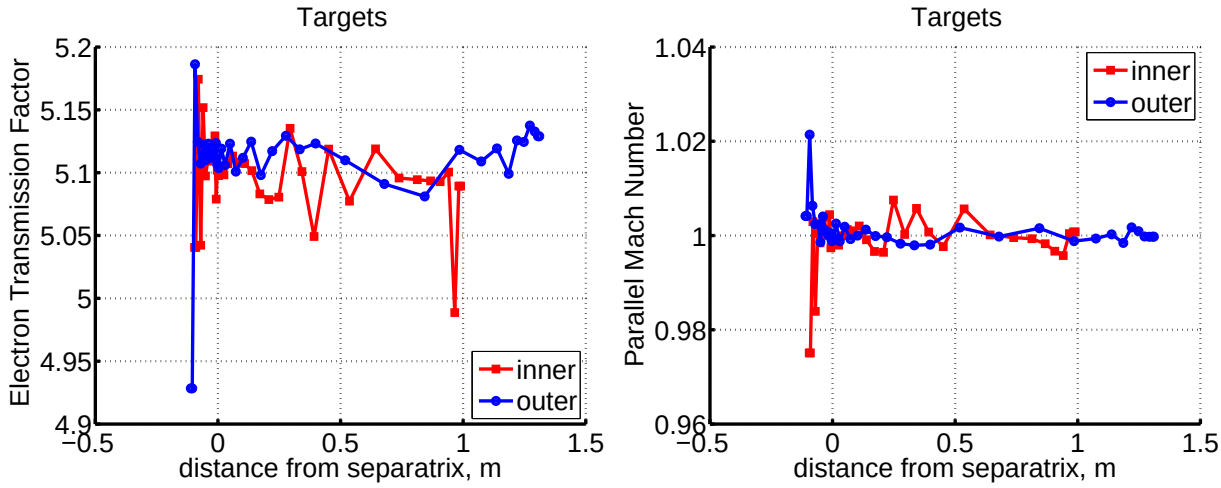

(a) (b)

Figure 6.15: a) electron sheath transmission factor, see caption of Figure 6.5, and b) parallel Mach number at the divertor targets, obtained for the test case '1e-4x40*' (#1542vk4)

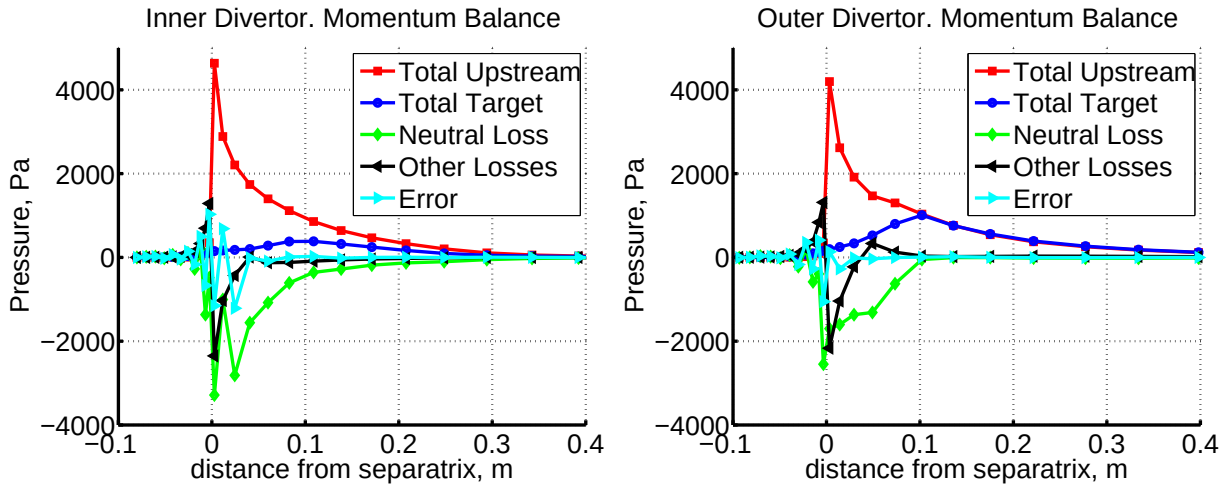

(a) (b)

Figure 6.16: Diagrams of the integral (parallel) momentum balance, see [15], in the divertor legs, case '1e-4x40*', #1542vk4

Table 6.8: Average CPU time (sec) required for one time-iteration

	1e-4x1	1e-4x10	1e-4x40	1e-4x40*	2e-7x1	2e-7x10
CFD	15	15	15	7.0	5.5	5.6
MC	29	261	1041	1033	29	260

The measurements are made on the workstations with Intel Xeon 2.67 GHz processors with 12 computing cores. In this table average (real) time consumed in the CFD part (B2) and in the Monte-Carlo part (EIRENE) is shown. Position "MC" in the table also includes the pre- and post-processing time of EIRENE. The Monte-Carlo part of the code is fully parallelized whereas CFD part runs on only one processor. The measured times are averaged over several hundred last time-iterations. The last stage 1e-4x40* was also run on the supercomputer JUROPA, with MC part parallelized on 128 processors. In this case the MC part takes 81 sec, and the CFD part takes 6.8 sec. The entire numerical experiment described in the present section took approximately 2 weeks of wall-clock time: including waiting time on the supercomputer and excluding runs with Δt=2e-7 sec.

Summary and outlook

1. Generalized residual *GENRES* has been introduced for the CFD-MC combination, which consists of the standard CFD residual R, plus inconsistency of source terms ΔS and ther statistical uncertanty

2. Internal iterations of the CFD solver are required to reduce R, thus *GENRES*, on each time-iteration, but they pose a severe restriction on the time-step ($\Delta t \approx$1e-7..1e-6 sec)

3. Much larger time-steps ($\Delta t \sim$1e-4 sec) can be used if internal iterations are not applied. However, a significant increase of the number of MC particles or time-averaging of source terms has to be used in this case to reduce *GENRES* to the same level as with internal iterations

4. Global particle balance represents a special issue which is not reflected in *GENRES* and has to be controlled separately.

5. It has been shown that without internal iterations the error in particle balance already due to the CFD residual alone can be larger than the particle throughput which controls the system. In this case the solution is driven into completely wrong direction

6. Extra correction of the particle-balance - "continuity iterations" - has been implemented and tested

7. It is found that the continuity iterations work well in bringing the solution into the correct parameter range even with a small number of MC particles. Increased number of MC particles (by a factor of 10-40 in the studied tests) is still required to bring *GENRES* down to the same level as with internal iterations

8. Continuity iterations lead to larger residuals of other equations, especially of those for momentum balance. Whereas in the low density (low throughput) ITER model this increase is moderate, in the high throughput case R for momentum balance is increased by more than a factor of 2 and is not reduced even with increased number of MC particles

9. With high particle throughput the continuity iterations are less critical than in the low density cases because with increased number of MC particles the relative error in the particle balance gets small enough even if extra correction is not applied. Therefore, in this case the continuity iterations can be used to get an initial approximation of the solution with small number of MC particles, and then be switched off on the "refinement" phase with large number of MC particles. Also, their use can be restricted to individual species, e.g. He

10. There is no strict estimate for the accuracy of final solution itself. The best level of *GENRES* which has been practically achieved for the ITER cases studied here is $\lesssim$0.1 for particle and electron energy balance, and $\lesssim$1 for ion energy and momentum balance of main ions. For this level of *GENRES* plasma profiles calculated with and without internal iterations are very close to each other

11. Convergence of the momentum balance of impurities is always bad. Even with internal iterations *GENRES*$\sim$1 for those equations, and can be much larger than 1 if internal iterations are not applied

12. It has been observed that the total number of time iterations required to reach the steady-state could be determined by the particle balance of He. Treating He in a separate model as a trace-impurity on the plasma background calculated by B2-EIRENE could make the convergence of ITER simulations substantially easier, while still being sufficiently accurate from the physics point of view

Bibliography

[1] Kukushkin A S *et al.* 2011 *Fus. Eng. Des.* **86** 2865

[2] Reiter D, Baelmans M and Börner P 2005 *Fus. Sc. Tech* **47** 172

[3] D'haeseleer W D, Pacher H D and Pacher G W 1992 *Contrib. Plasma Phys.* **32** 444

[4] Maddson G P and Reiter D 1994 *Recycling source terms for edge plasma fluid models and impact on convergence behaviour of the BRAAMS "B2" code* Report Jül-2872

[5] Kawashima H *et al.* 2006 *Plasma and Fusion Research* **1** 031

[6] Braams B J 1986 *Computational studies in tokamak equilibrium and transport* Ph.D. thesis Rijksuniversiteit Utrecht

[7] Braams B J 1992 *A Multi-Fluid Code for Simulation of the Edge Plasma in Tokamaks* Report on the NET contract 142/83-11/FU-NL/NET

[8] Baelmans M 1993 *Code improvements and applications of a two-dimensional edge plasma model for toroidal fusion devices* Ph.D. thesis Katholieke Universiteit Leuven

[9] Braginskii S I 1965 *Reviews of Plasma Physics* vol. 1 p. 205 (New York: Consultants Bureau)

[10] Patankar S V 1980 *Numerical heat transfer and fluid flow* (Hemisphere Publishing Corporation, New York)

[11] Hodges J L and Lehmann E L 1964 *Basic concepts of probability and statistics* (Holden-Day Inc., San Francisco)

[12] Ortega J M and Rheinboldt W C 1970 *Iterative solution of nonlinear equations in several variables* (Academic Press, New York and London)

[13] Feng Y, Lunt T, Kukushkin A S *et al. EMC3-Eirene/SOLPS4.3 comparison for ITER* 38th EPS Conference on Plasma Physics, Strasbourg, France, 27 June - 1 July 2011, ECA Vol.35G, P1.071

[14] Kotov V *et al.* 2008 *Plasma Phys. Control. Fusion* **50** 105012

[15] Kotov V and Reiter D 2009 *Plasma Phys. Control. Fusion* **51** 115002

Appendix: references in SOLPS4.3 (FZJ) and technical notes

The generalized residuals diagnostic (*GENRES*) in B2 , Section 2.2, is implemented in `diagno/b2efres.F`. It produces the tracing file `tracing/efres.trc`. Standard deviations required in Equation (2.10) are transferred from EIRENE through module EIRBRA (arrays `SDV_???`). In EIRENE they are calculated in `infstat.f`. The option is switched on by defining `NSIGI_COP=-1` is Block 9 of EIRENE input file.

The CFD residual for this diagnostic is calculated by an empty run of `B2CEPS` after all internal iterations are completed. That is, a run with `rxfi=0` to skip update of the solution and `tol=0.1` and `tol1=0.1` to make fast runs of the matrix solvers. Extra empty run of `B2CEPS` is switched on if `l_repeat_res=t` (namelist `DIAGNOSTICS`). Also, last time-iteration of B2 can be skipped to print the solution which corresponds exactly to the last call of EIRENE (switch `skip_last_b2ceps`).

The particle balance diagnostic discussed in Section 5.1 is implemented in `diagno/b2erbal.F`. It produces tracing file `tracing/erbal.trc`. Due to technical reasons, the results of both *GENRES* and the particle balance diagnostic can be distorted if limitation of the negative source terms is applied, see Section 5.4. It is therefore recommended not to use the source limitation together with those diagnostics, that is, to set `time_factor_required=0.0`.

Time averaging described in Section 3 is performed in B2 in `neutrals/neutrals.F`, in the subroutine `AVERAGE_EIR_SOURCES_CONV`. The number of particles in EIRENE is changed from B2 through the interface `EIRENE_CHANGE_NPTS` (in `infcop.f`). The option is switched on if `leavr=1` in the namelist `NEUTRALS`. `NEAVR2` is the length of averaging phase - parameter L of Section 3; `fmcfirst` is the multiplicator for the number of Monte-Carlo particles applied at the end of the averaging phase; `l_norm_avr_???` switches between Equation (3.1) and Equation (3.2).

Extra iterations for correction of particle balance described in Section 5.2 are implemented technically as the same calls of `B2CEPS` as for the regular (full) internal iterations but with correction of all equations except continuity equations skipped, and for those latter `rxfi=1.0` is applied. Internal iterations after the first one are treated in this way if `CONTINUITY_ITERATIONS=t` in namelist `NUMERICS`. Logical switches `LXMOMPART` allow to select individual ion fluids to which the correction procedure is applied.

The pure upwind scheme for continuity equation, see Section 5.2, is implemented in `B2CCON`. The default modified upwind scheme is switched to pure upwind if `L_PUREUPWIND=t`. This same switch actives modified implementation of the boundary condition `BCCON=3` in `SRCBND`, and implicit treatment of the radial diffusion term. For this latter corrections are implemented in both `PHYDIF` and `B2CCON`.

A mistake has been found in the subroutine `FD2EQN` which calculates coefficients of the 5-points equations: `ASO`, `AWE`, `ACP`, `AEA`, `ANO`. To fix the bug, a patch has been implemented in `B2CCON` which corrects the coefficients after call of `FD2EQN`. The fix is activated when `L_FIX_FD2EQN=t`. Similar fix has been made for the energy balance equations in `B2CENE`, activated when `L_FIX__FD2EQN_B2CENE=t`. All calculations discussed in the present report are made with `L_PUREUPWIND=t`, `L_FIX_FD2EQN=t`, `L_FIX__FD2EQN_B2CENE=t`.

The test options described in Section 5.3 are introduced in `B2CCON`, they are activated by switching `LB2CCON_RES2=t` and `L_TEST_PRCOR=t`.

Automatic reduction of time-step, Section 5.4, is performed in `USERDT` if `DFLAGDT`<0. The subroutine is called in `B2CCON` and in `B2CSRC` - for initialization.

Simplified correction of the CFD particle balance, Section 5.5, can be found in `user/scale_ni.F`. The subroutine is called in `B2DRIV` after call of `B2CEPS` (the implementation is intended for use only with one internal iteration). The number of iterations in `SCALE_NI` is defined by variable `NSCALE_NI`.

Jül-4371
Februar 2014
ISSN 0944-2952